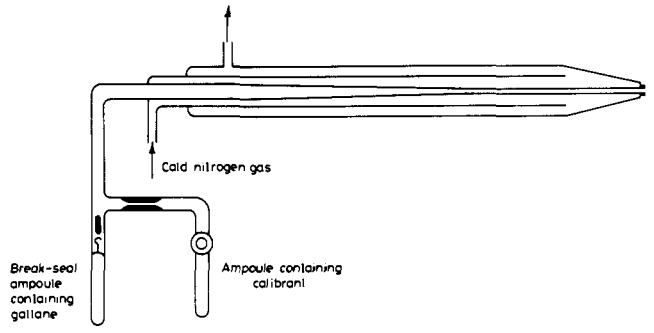

Figure 11. All-glass inlet system used for the admission of gallane vapor to the chamber of the electron-diffraction apparatus.

ter with the scanning program described previously.[57] Calculations made use of well-established programs for data reduction[57] and least-squares refinement,[35] the complex scattering factors being those listed by Fink and Ross.[58]

Chemical Studies and Reagents. The thermal instability of gallane made it impossible to determine the mass of a sample prior to any chemical reaction. Hence it was necessary, as in the experiment with HCl (q.v.), to treat the sample with a measured quantity of the reagent, judged to be in excess, under the appropriate conditions, then to separate and identify the components of the reaction mixture (typically on the basis of their vibrational and/or NMR spectra), and, where appropriate, to assay one or more of these components (e.g., by manometric measurements or elemental analysis). The reaction itself was carried out in a preconditioned all-glass ampoule equipped with a break-seal, in accordance with the sort of procedures that were adopted for the synthesis and isolation of the gallane (q.v.); subsequent manipulation and analysis of the reaction mixture could usually be accomplished using a more conventional vacuum line having a distillation train and greased ground-glass or, if necessary, greaseless stopcocks as well as ground-glass joints lubricated typically with Apiezon L grease. In none of the experiments was there any evidence that unchanged gallane survived the encounter with an excess of the reagent (HCl, NMe_3, NH_3, PH_3, or C_2H_4) under the conditions outlined in the preceding section.

All noncondensable gases—Ar, Kr, and N_2 (research grade)—were used as received from the British Oxygen Co. (B.O.C.). The following reagents, from the commercial sources indicated, were purified before use by fractionation in vacuo: HCl (Air Products), NH_3 (B.O.C.), and C_2H_4 (B.O.C.). Toluene-d_8 and benzene-d_6, both supplied by Aldrich, were dried and fractionated in vacuo prior to use as NMR solvents. Phosphine was prepared by the action of aqueous hydrochloric acid on calcium phosphide (Ventron), trimethylamine by the action of alkali on trimethylammonium chloride (Aldrich); fractional condensation of each of these reagents in vacuo gave a sample judged to be pure by the criteria of tensimetric and IR measurements.

Acknowledgment. This work was supported by the S.E.R.C. through a research grant, through the award of research studentships (to M.J.G. and C.R.P.), through funding of the Edinburgh Electron-Diffraction Service (including H.E.R.'s research assistantship), and through provision of the microdensitometer facilities at Daresbury. We thank Professor I. M. Mills for much practical assistance and advice concerning the IR spectrum and vibrational analysis of Ga_2H_6, and also acknowledge with gratitude the contributions of Dr. P. L. Baxter (who carried out the early experiments with gallium(III) chloride and metal tetrahydridogallates) and Mr. P. T. Brain (for assistance with the NMR measurements).

(57) Cradock, S.; Koprowski, J.; Rankin, D. W. H. *J. Mol. Struct.* **1981**, *77*, 113.
(58) Fink, M.; Ross, A. *International Tables for Crystallography*; International Union of Crystallography; Reidel: Dordrecht, in press.

Spectroscopic Studies of the Non-Heme Ferric Active Site in Soybean Lipoxygenase: Magnetic Circular Dichroism as a Probe of Electronic and Geometric Structure. Ligand-Field Origin of Zero-Field Splitting

Yan Zhang, Matthew S. Gebhard, and Edward I. Solomon*

Contribution from the Department of Chemistry, Stanford University, Stanford, California 94305.
Received October 15, 1990

Abstract: Ferric active sites are found in non-heme, non-iron–sulfur enzymes performing a variety of biological functions often involving dioxygen activation. Soybean lipoxygenase (SBL) is an important member of this class catalyzing the hydroperoxidation of unsaturated lipids. The purpose of this study is to use the combination of EPR and variable temperature variable field magnetic circular dichroism (MCD) to probe the ground and excited states in high-spin non-heme ferric enzymes. Low-temperature MCD is used to observe the low-energy spin-forbidden ligand-field excited states that are not obscured by higher energy charge transfer (CT) transitions. Parallel studies on ferric model complexes and predictions of *C*-term signs and transition energies are presented which enable the ferric geometry to be estimated from these ligand-field spectral features. Saturation magnetization of the MCD bands associated with CT transitions provides polarization information and thus the orientation of the ligand–Fe(+3) bonds relative to the **g** tensor of the ground doublet which is determined by the zero-field-splitting (ZFS) tensor. Variable-temperature EPR and MCD are used to obtain the ground-state ZFS which is analyzed in terms of the ligand field at the Fe(+3) site. Here we extend our earlier treatment of distorted tetrahedral complexes (Deaton, J. C.; Gebhard, M. S.; Koch, S. A.; Millar, M.; Solomon, E. I. *J. Am. Chem. Soc.* **1988**, *110*, 6241) to distorted octahedral and five-coordinate complexes. Together the saturation magnetization MCD and ZFS analyses enable one to obtain the orientation of specific chromophoric ligands at the active site. This is used to probe both endogenous and exogenous ligand to Fe(+3) CT transitions and provides significant geometric information. Studies of Fe(+3)-SBL show that oxidation of the octahedral Fe(+2) site produces little change in the coordination sphere of the iron center, which likely has at least two histidine ligands in a cis configuration which define the equatorial plane. OCN^- and N_3^- bind to the ferric active site producing rhombic EPR signals which parallel those observed upon hydroperoxide product addition to ferric enzyme. The MCD studies of the associated CT transitions define exogenous ligand interactions with the ferric SBL active site which are of relevance to the catalytic mechanism.

Introduction

Mononuclear non-heme iron centers are known or believed to be present in the catalytic active site of a large number of enzymes involved in reactions with dioxygen. These enzymes include the following: soybean lipoxygenase (SBL, hydroperoxidation of unsaturated lipids),[1a] Fe superoxide dismutase (SOD, dismutation

0002-7863/91/1513-5162$02.50/0

of superoxide),[1b] phenylalanine hydroxylase (tetrahydropterin dependent hydroxylation of aromatic rings),[1c] extradiol and intradiol dioxygenases (catechol ring cleavage),[1d] α-ketoglutarate dioxygenases (hydroxylation of pyrimidines and nucleosides),[1e] and ω-hydroxylase (hydroxylation of alkanes and fatty acids).[1f] Both the ferric and the ferrous oxidation states have been implicated in the different enzyme reaction mechanisms.[1] An understanding of the reactivity of these enzymes requires knowledge of the coordination environment of the active site. However, crystal structures are presently only available for SOD[2] and the intradiol dioxygenase, protocatechuate 3,4-dioxygenase.[3] Therefore both geometric and electronic structural insight into these active sites and their interactions with substrates and small molecules of relevance to catalysis must be derived from spectroscopic methods.

Ferrous active sites have been the least studied as they are not easily accessible through the usual methods of absorption and EPR. Recently, a spectroscopic protocol for the study of ferrous active sites in non-heme metalloenzymes has been developed by using a combination of absorption (Abs), circular dichroism (CD), and magnetic circular dichroism (MCD) spectroscopies, each method having different selection rules.[4] This combination of spectroscopies permits observation of transitions to ligand-field excited states. The temperature and field dependence of the intensity of the MCD signal of these bands further probes the ground state of the ferrous center. This approach permits construction of an experimental ligand-field energy-level diagram for the ferrous center providing detailed insight into the geometric and electronic structure. To date, this protocol has proven to be extremely useful in the study of the ferrous active sites in SOD, SBL,[4] and metapyrocatechase, an extradiol dioxygenase.[5]

The non-heme ferric active sites are readily accessible through EPR and absorption spectroscopy. The high-spin d^5 ground state is $^6A_1$ which undergoes a zero-field splitting (ZFS) as defined by eq 1

$$\mathcal{H} = D[S_z^2 - \tfrac{1}{3}S(S+1)] + E(S_x^2 - S_y^2) \qquad (1)$$

where D is the axial and E the rhombic spin Hamiltonian parameter. In the case of axial complexes ($E/D \sim 0$) this Hamiltonian generates three doublets, $M_S = \pm^1/_2, \pm^3/_2, \pm^5/_2$, split by $2D$ and $4D$ with the EPR signal arising from the $\pm^1/_2$ doublet with $g_\parallel = 2.0$ and $g_\perp = 6.0$. For a completely rhombic site ($E/D = 1/3$) one obtains three equally spaced doublets (by an amount $Z = 3.5D$) with the EPR intensity deriving from the middle doublet[6] which has an approximately isotropic g value of 4.3. The ground-state g values yield the E/D ratio while the temperature dependence of the EPR signal gives the doublet splittings and therefore the axial ZFS, D. These spin Hamiltonian parameters are related through ligand-field theory to molecular properties, yet their information content has not been developed. Griffith[7] has derived an expression relating the ZFS to the low-symmetry splitting of the first-excited $^4T_1$ ligand-field state. However we have recently tested this experimentally[8] for tetrahedral complexes and found this model to predict the wrong sign and magnitude of the ZFS, and we have determined that this discrepancy derives from the differences in covalency of the different d orbitals. This contribution has not been evaluated for octahedral or five-coordinate complexes.

The absorption (and CD) spectra of high-spin d^5 complexes are dominated by the spin-allowed ligand-to-Fe(+3) charge-transfer (CT) transitions from the more easily oxidized ligands. The ligand-field (LF) transitions, which provide a sensitive probe of geometry, are all spin-forbidden $^6A_1 \rightarrow {}^4\Gamma$ (where $^4\Gamma = {}^4T_1$, $^4T_2$, ... in order of increasing energy) and thus are very weak in absorption and have not yet been observed in any mononuclear non-heme Fe(+3) enzyme. Enzymes such as Fe(+3)SOD[1b] and Fe(+3)SBL[1a] exhibit a moderately intense absorption band ($\epsilon \approx 2 \times 10^3$ M^{-1} cm^{-1}) at ~350 nm which, based on the ligands determined by the X-ray structure[2] of Fe(+3)SOD, are likely His $\rightarrow$ Fe(+3) CT transitions although carboxylate could also make some contribution to this region.[9] Exogenous ligand binding to the Fe(+3) site can produce further excited-state spectral changes. From results on Fe(+3)SOD, F^- binding perturbs the existing 350-nm CT transition, while N_3^- binding results in a new intense $N_3^- \rightarrow$ Fe(+3) CT transition at 440 nm ($\epsilon = 1.7 \times 10^3$ M^{-1} cm^{-1}).[1b,10] For SBL, the hydroperoxide product interacts with the ferric enzyme to produce a purple derivative which exhibits an intense transition at 570 nm ($\epsilon = 1.3 \times 10^3$ M^{-1} cm^{-1}) and is thought to be a new endogenous ligand-to-Fe(+3) CT transition.[11]

MCD spectroscopy provides a powerful probe of the ground and excited states. First, MCD can be more effective than absorption spectroscopy in observing spin-forbidden ligand-field excited states. This derives from the greater instrumental sensitivity of the method, the high C-term MCD intensity at low temperature associated with paramagnetic ground states, the larger C/D ratio (the ratio of MCD C-term intensity to the square of the transition dipole strength) expected for LF relative to CT excited states based on spin–orbit coupling mechanisms, and the fact that a MCD transition has a sign as well as magnitude which can help resolve it from overlapping intense CT bands. Further, MCD can be used to obtain polarization information on a CT excited state even for an orientation averaged frozen solution through analysis of the saturation behavior of the MCD signal of a transition at low temperature and high magnetic field. The idea here is that C-term MCD intensity requires two perpendicular electronic transition moments which project out a specific (orthogonal) g value of the ground doublet. It is this g value which determines the Zeeman splitting of the doublet contributing to the MCD intensity and hence its magnitude with field and temperature. Schatz et al.[12] derived expressions for this saturation behavior in axial symmetry ($g_x = g_y \neq g_z$) and Thomson and Johnson[13] demonstrated its utility and further developed the analysis to account for rhombic g values ($g_x \neq g_y$) from transitions with known polarization in heme proteins. Bennett and Johnson[14] have applied the saturation magnetization treatment to the iron sulfur protein, rubredoxin, to show that the polarization of a transition can be obtained from an orientation averaged glass which agrees with results obtained from single crystal absorption studies. Stephens et al.[15] have shown that the temperature de-

(1) (a) Veldink, G. A.; Vliegenthart, J. F. G. *Adv. Inorg. Biochem.* **1984**, *6*, 139. (b) Slykhouse, T. O.; Fee, J. A. *J. Biol. Chem.* **1976**, *251*, 5472. (c) Shiman, R. *Folates and Pterins* Wiley: New York, 1984; Vol. 2, pp 179–249. (d) Nozaki, M. *Top. Current Chem.* **1979**, *78*, 145. (e) Warn-Cramer, B. J.; Macrander, L. A.; Abbott, M. T. *J. Biol. Chem.* **1983**, *258*, 10551. (f) Ruettinger, R. T.; Griffith, G. R.; Coon, M. J. *Arch. Biochem. Biophys.* **1977**, *183*, 528.

(2) (a) Stallings, W.; Bull, C.; Pattridge, K. A.; Powers, T. B.; Fee, J. A.; Ludwig, M. L.; Ringe, D.; Petsko, G. A. *Oxygen Radicals in Chemistry and Biology*; Water de Gruyter & Co.: Berlin, Germany, 1984; pp 779–792. (b) Stallings, W.; Bull, C.; Pattridge, K. A.; Ludwig, M. L. *Superoxide and Superoxide Dismutase in Chemistry*; Elsevier: New York, 1986; pp 195–201.

(3) Ohlendorf, D. H.; Lipscomb, J. D.; Weber, P. C. *Nature* **1988**, *336*, 403.

(4) (a) Whittaker, J. W.; Solomon, E. I. *J. Am. Chem. Soc.* **1986**, *108*, 835. (b) Whittaker, J. W.; Solomon, E. I. *J. Am. Chem. Soc.* **1988**, *110*, 5329.

(5) Mabrouk, P. A.; Orville, A.; Lipscomb, J. D.; Solomon, E. I. *J. Am. Chem. Soc.* Submitted for publication.

(6) Gibson, J. F. In *ESR and NMR Paramagnetic Species in Biological and Related Systems*; Bertini, I., Drago, R. S., Ed.; Reidel: 1979; pp 225–253.

(7) (a) Griffith, J. S. *Biopolym. Symp.* **1964**, *1*, 35. (b) Griffith, J. S. *Mol. Phys.* **1964**, *8*, 213.

(8) (a) Deaton, J. C.; Gebhard, M. S.; Solomon, E. I. *Inorg. Chem.* **1989**, *28*, 877. (b) Gebhard, M. S.; Deaton, J. C.; Koch, S. A.; Millar, M.; Solomon, E. I. *J. Am. Chem. Soc.* **1990**, *112*, 2217.

(9) It should be noted that the intradiol dioxygenases also have intense transitions ($\epsilon \sim 10^4$ M^{-1} cm^{-1}) at ~450 nm which are endogenous tyrosine $\rightarrow$ Fe(+3) CT. (Whittaker, J. W.; Lipscomb, J. D.; Kent, T. A.; Munck, E. *J. Biol. Chem.* **1984**, *259*, 4466.)

(10) Dooley, D. M.; Jones, T. F.; Karas, J. L.; McGuirl, M. A.; Brown, R. D., III; Koenig, S. H. *J. Am. Chem. Soc.* **1987**, *109*, 721.

(11) Slappendel, S.; Veldink, G. A.; Vliegenthart, J. F. G.; Aasa, R.; Malmstrom, B. G. *Biochim. Biophys. Acta* **1983**, *747*, 32.

(12) Schatz, P. N.; Mowery, R. L.; Krausz, E. R. *Mol. Phys.* **1978**, *35*, 1537.

(13) Thomson, A. J.; Johnson, M. K. *Biochem. J.* **1980**, *191*, 411.

(14) Bennett, D. E.; Johnson, M. K. *Biochim. Biophys. Acta* **1987**, *911*, 71.

(15) Browett, W. R.; Fucaloro, A. F.; Morgan, T. V.; Stephens, P. J. *J. Am. Chem. Soc.* **1983**, *105*, 1868.

Table I

	EPR[a]						VT MCD[a]	
	g_x	g_y	g_z	Z, cm^{-1}	D, cm^{-1}	E/D	Z, cm^{-1}	D, cm^{-1}
native Fe(+3)SBL	6.21	5.84	2.0	N.A.	1.7 ± 0.5	0.01	N.A.	1.5 ± 0.5
Fe(+3)SBL–OCN^-	(1.36)	9.44	(0.88)	4.7 ± 0.5	(1.3 ± 0.5)	0.27	4.0 ± 0.5	(1.1 ± 0.5)
Fe(+3)SBL–N_3^-	(0.86)	(9.68)	(0.61)			0.33		

[a] Values in parentheses are calculated.

pendence of the MCD signal at fixed low field can be used to probe Boltzmann population of excited sublevels of the ground state and hence can be used to obtain a complementary estimate of the ZFS which is not complicated by EPR relaxation effects.

The purpose of this study is to use the combination of EPR and variable-temperature variable-field (VTVH) MCD to probe the ground and excited states in high-spin non-heme ferric enzymes. Low-temperature (LT) MCD is used to obtain the lowest energy ligand-field excited states which are not obscured by higher energy CT transitions. Parallel studies on model complexes and predictions of *C*-term signs and transition energies are presented which enable the ferric structure to be estimated from these ligand-field spectral features. Saturation magnetization of CT transitions provides polarization information and thus the orientation of the ligand–Fe(+3) bonds relative to the **g** tensor of the ground doublet which is determined by the ZFS tensor. Variable-temperature (VT) EPR and MCD are used to obtain the ground-state ZFS which is analyzed in terms of the ligand field at the Fe(+3) site. Here we extend our earlier treatment[8] to octahedral and five-coordinate complexes. Together the saturation magnetization MCD and ZFS analyses enable the orientation of specific chromophoric ligands at the active site to be obtained. This is used to probe both endogenous and exogenous ligand-to-Fe(+3) CT transitions and provides significant geometric information of relevance to the catalytic mechanism. This approach is applied to probe the ferric active site geometric and electronic structures of soybean lipoxygenase, a non-heme iron enzyme for which the ferric oxidation state has been implicated in catalysis. While Fe(+3)SBL is the focus of this study, the protocol presented here should be generally applicable to other non-heme iron enzymes where the ferric site is of mechanistic importance.

SBL catalyzes the peroxidation of 1,4-unsaturated lipids and plays an important role in unsaturated fatty acid metabolism.[1a] The enzyme contains one non-heme iron center per 94 000 D.[16] The iron in the resting form of the enzyme isolated from soybean is in the ferrous oxidation state and must be activated by oxidation to the ferric state. Two mechanisms have been proposed for catalysis.[17] The first involves the reduction of the ferric ion by substrate to form a ferrous–fatty acid radical intermediate which reacts with dioxygen to form the peroxide product with reoxidation of the ferrous center. The second mechanism proposes that Fe(+3) facilitates the deprotonation of the substrate by forming a ferric–substrate organometallic intermediate followed by insertion of molecular oxygen.

A number of structural studies have been reported on the ferrous form of lipoxygenase. MCD has shown that the ferrous active site has a 6-coordinate distorted octahedral geometry.[4] EXAFS indicates the presence of 4 ± 1 imidazole nitrogens and 2 carboxylate oxygens at the ferrous site.[18]

Limited information about the coordination and geometry of the ferric active site has been reported. As indicated above, ferric SBL exhibits a charge-transfer band at 350 nm ($\epsilon \approx 2200$ M^{-1} cm^{-1}) and has an axial EPR spectrum[1a] with $g_\parallel \approx 2.0$ and $g_\perp \approx 6$. The hydroperoxide product bound purple form exhibits a rhombic EPR signal[1a] with $g \sim 4.3$. H_2O[17] binding studies have shown that this ligand is likely coordinated to the ferric active site.[19] Iron XANES[20] indicates a coordination number of 6 or 7. The studies reported here use EPR and VTVH MCD to probe this ferric active site and its interaction with small molecules which model the hydroperoxide product interaction with the active site.

Experimental Section

Soybean lipoxygenase (SBL) was purified from soybeans (Williams Variety, Tabor Seed Division, Decatur, IL) following previously reported procedures.[4] Enzyme activity was determined by monitoring the absorption of the product formed during the enzymatic reaction at 234 nm ($\epsilon_{234} = 2.5 \times 10^4$ M^{-1} cm^{-1}). The metal content of the enzyme was determined by atomic absorption analysis with a Perkin-Elmer Model 2380 graphite furnace AA spectrometer. The minimum specific activity of the enzyme was 100–140 units/mg. The average iron content was (0.8–1.0) ± 0.1 mol of Fe/mol of enzyme. The enzyme was homogeneous based on SDS gel electrophoresis. Ferric SBL was generated by the addition of a stoichiometric amount of the peroxide product, (9*Z*,11*E*)-13-hydroperoxy-9,11-octadecadienoic acid, to the native ferrous enzyme.[21] The product was obtained according to published procedures.[22] The anion bound forms of Fe(+3)-SBL were obtained by direct addition of a 50–150-fold excess of anion (N_3^- or OCN^-) to Fe(+3)-SBL in 0.1 M sodium borate buffer, pH = 9.0.

Ferric complexes, potassium (ethylenediaminetetraacetato)ferrate(III)[23] $[FeEDTA\cdot H_2O]^-$, potassium tris(oxalato)ferrate(III)[24] $[Fe(OX)_3]^{3-}$, tetraphenylarsonium pentaazidoiron(III)[25] $[Fe(N_3)_5]^{2-}$, and ferric tetrachloride[8a] $[FeCl_4]^-$, were prepared according to the published procedures. All chemicals used in the synthesis of these complexes were reagent grade or better and were used without further purification.

The UV–vis absorption spectra were recorded on a Cary 17 spectrophotometer. Circular dichroism spectroscopy was performed on a Jasco J-500 spectropolarimeter operating with S-1 and S-20 photomultipliers in the 1100–800- and 900–300-nm regions, respectively. Low-temperature magnetic circular dichroism data were acquired with the same spectropolarimeter, equipped with an Oxford Instruments SM-4 superconducting magnet[26] which is capable of magnetic fields up to 6.0 T and temperatures down to 1.6 K. EPR spectra were obtained on a Bruker ER 220-D SRC spectrometer with a Lake Shore cryotronics temperature controller Model DTC-500. The microwave frequencies were measured with a Hewlett-Packard Model X532B frequency meter. The *g* values are accurate to ±0.05.

Protein samples were prepared for MCD study by dialyzing the enzyme against a 1:1 (by volume) mixture of 0.2 M sodium borate buffer (pH = 9.0) and glycerol. EPR spectra show no significant changes with the addition of glycerol. The samples were inserted slowly into the cryostat to reduce the strain of the resulting frozen optical glass. The depolarization of the protein glass was checked by measuring the CD of a freshly prepared nickel tartrate solution placed immediately before and after the MCD sample.[15] All samples studied exhibited <5% depolarization at 4 K. Mulls of the model complexes were prepared for MCD study by grinding the crystals in mineral oil. An optically transparent layer of the resulting mull was sandwiched between two quartz disks. The EPR temperature-dependence data were collected at non-power saturation conditions, which were determined by power vs intensity experiments at the lowest temperature. As the line width does not appear to broaden appreciably in the temperature range used,[27] the EPR in-

(16) Shibata, D.; Steczko, J.; Dixon, J. E.; Hermodson, M.; Yazdanparast, R.; Axelrod, B. *J. Biol. Chem.* **1987**, *262*, 10080.
(17) (a) Feiters, M. C.; Aasa, R.; Malmström, B. G.; Slappendel, S.; Veldink, G. A.; Vliegenthart, J. F. G. *Biochim. Biophys. Acta* **1985**, *831*, 302. (b) Corey, E. J.; Nagata, R. *J. Am. Chem. Soc.* **1987**, *109*, 8107. Corey, E. J.; Walker, J. C. *J. Am. Chem. Soc.* **1987**, *109*, 8108.
(18) Navaratnam, S.; Feiters, M. C.; Al-Hakim, M.; Allen, J. C.; Veldink, G. A.; Vliegenthart, J. F. G. *Biochim. Biophys. Acta* **1988**, *956*, 70.
(19) Nelson, M. J. *J. Am. Chem. Soc.* **1988**, *110*, 2985.
(20) Roe, A. L.; Hodgson, K. O.; Reem, R. C.; Whittaker, J. W.; Solomon, E. I. Unpublished results.
(21) Slappendel, S.; Veldink, G. A.; Vliegenthart, J. F. G.; Aasa, R.; Malmström, B. G. *Biochim. Biophys. Acta* **1981**, *667*, 77.
(22) Verhagen, J.; Veldink, G. A.; Egmond, M. R.; Vliegenthart, J. F. G.; Boldingh, J.; van der Star, J. *Biochim. Biophys. Acta* **1978**, *529*, 369.
(23) Lind, M. D.; Hamor, M. J.; Hamor, T. A.; Hoard, J. L. *Inorg. Chem.* **1964**, *3*, 34.
(24) Clark, H. C.; Curtis, N. F.; Odell, A. L. *J. Chem. Soc.* **1954**, 63.
(25) Drummond, J.; Wood, J. S. *Chem. Commun.* **1969**, 1373.
(26) Spira-Solomon, D. J.; Allendorf, M. D.; Solomon, E. I. *J. Am. Chem. Soc.* **1986**, *108*, 5318.
(27) Slappendel, S.; Veldink, G. A.; Vliegenthart, J. F. G.; Aasa, R.; Malmström, B. G. *Biochim. Biophys. Acta* **1980**, *642*, 30.

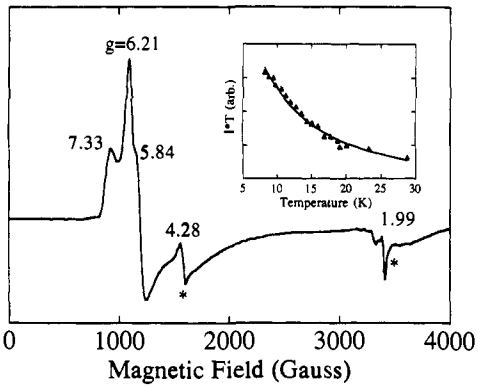

Figure 1. EPR spectrum of 0.5 mM Fe(+3)SBL at 4.5 K. The asterisks indicate advantageous Fe(+3) at $g \sim 4.3$ and a Mn impurity in the $g \sim 2$ region. EPR parameters: microwave frequency, 9.52 GHz; power, 3.1 mW; modulation amplitude, 10 G. Inset shows the temperature dependence of the $g = 6.2$ EPR signal intensity. The EPR parameters used are the same as above. The EPR intensities were measured by the amplitudes of the $g = 6.2$ signal. Fit (—) obtained for population of three doublets separated by 3.4 and 6.8 cm^{-1}.

tensity was measured by the amplitude of a specific signal.

Results

A. Native Ferric SBL. (i) EPR. The ground-state properties of Fe(+3)SBL were studied by EPR spectroscopy. As shown in Figure 1, the EPR which reproduces published results[1a] is composed of overlapping features in the $g_\perp \approx 6$ spectral region with g values of 5.84, 6.21, and 7.33. Note that there is a small rhombic impurity at $g = 4.28$, and the $g_\parallel = 2$ region contains overlapping signals from a Mn contaminant.[1a] The E/D ratio estimated from the splitting of the observed $g_\perp$ region[28] is approximately 0.01. This indicates an axial ZFS of the $S = {}^5/_2$ ground state into three Kramers doublets, $M_S = \pm{}^1/_2\ \pm{}^3/_2$, and $\pm{}^5/_2$, split by $2D$ and $4D$, respectively. From the temperature dependence of the EPR intensity of the $g_\perp \approx 6$ signal (Figure 1 inset), the $M_S = \pm{}^1/_2$ must be the lowest doublet and $D = +1.7 \pm 0.5$ cm^{-1} consistent with the literature.[27] These ground-state data are summarized in Table I.

(ii) Ligand-Field Region. The low-temperature MCD spectrum of Fe(+3)SBL in the region from 500 to 1100 nm is presented in Figure 2A. There are three resolvable bands in the spectrum. The negative band at 570 nm and the positive band at 930 nm are indicated by asterisks. Control experiments over a series of protein preparations indicate that the 570-nm negative band can be correlated to the presence of a heme impurity (<1%). The positive band at 930 nm is due to residual unoxidized Fe(+2)SBL (ca. 5%). Since heme and ferrous centers have absorption coefficients orders of magnitude greater than that of the ferric center,[29] very small quantities of these impurities can cause significant interference with the ferric SBL transitions in this ligand-field spectral region. The weak negative band centered at 750 nm is found to be very reproducible over protein preparations and has an intensity and energy which is indicative of its assignment as a spin-forbidden d → d transition of the ferric active site.[30]

For comparison, the MCD spectra of a series of ferric model complexes with varying geometry have been recorded in the same

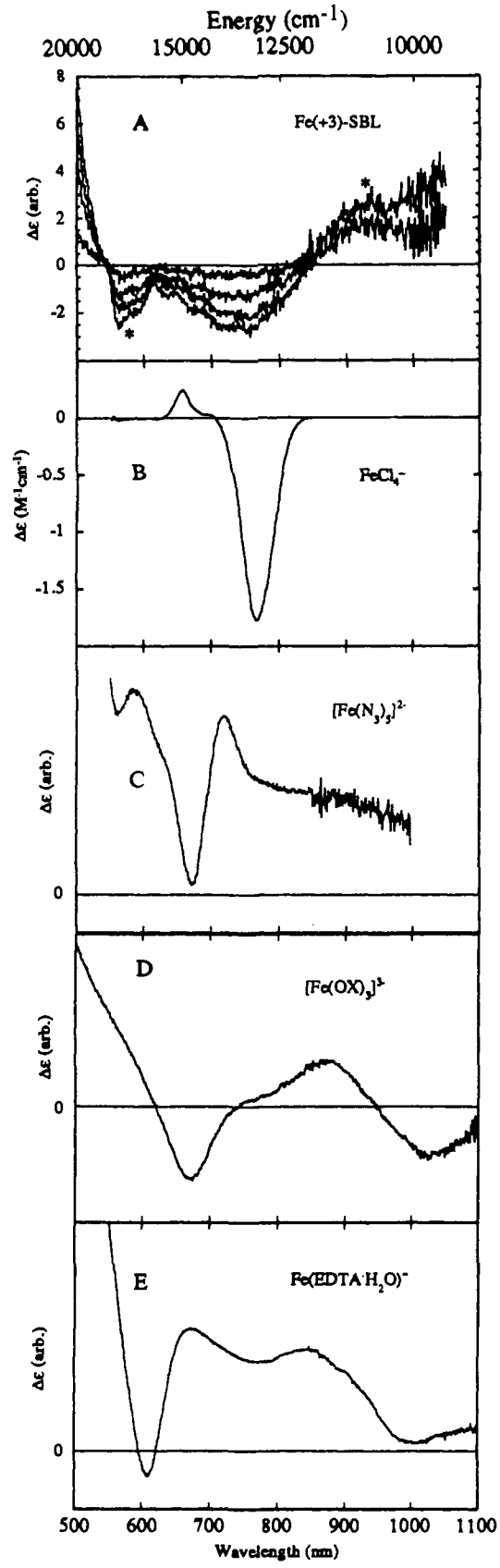

Figure 2. LT MCD ligand-field spectra (500–1100 nm) of Fe(+3)SBL and a series of model complexes. (a) 1.41 mM Fe(+3)SBL at 9.3 K and 1.0, 3.0, 4.0, and 6.0 T. Only spectra at 3.0 and 6.0 T are shown between 850 and 1100 nm. Cell path length was 3.0 mm. The asterisks indicate interfering signals due to the presence of heme and ferrous impurities. (b) Single-crystal $FeCl_4^-$ at 2.0 K and 6.0 T. (c) Mull of $Fe(N_3)_5^-$ at 4.2 K and 3.0 T. (d) Mull of $[Fe(OX)_3]^{3-}$ at 4.2 K and 3.0 T. (e) Mull of $Fe(EDTA{\cdot}H_2O)^-$ at 4.2 K and 3.0 T.

(28) More than one species are present in ferric SBL. (de Groot, J. J. M. C.; Veldink, G. A.; Vliegenthart, J. F. G.; Boldingh, J.; Wever, R.; van Gelder, B. F. *Biochim. Biophys. Acta* **1975**, *377*, 71.) $E/D = 0.01$ is from the major component. $E/D = 0.06$ is obtained from the $g \approx 7$ component. See ref 19.

(29) Lever, A. B. P. *Inorganic Electronic Spectroscopy*, 2nd ed.; Elsevier: New York, 1984.

(30) It should be noted that all spectral features reported in this study are reproducible over >20 sample preparations and have been determined to correspond to active Fe(+3) centers based on their correlation to EPR data. In particular, the zero field splitting and effective g values obtained from the temperature and field dependence of the MCD signal from each transition qualitatively correspond to the values for these parameters obtained from the EPR signals which correlate with the activity.

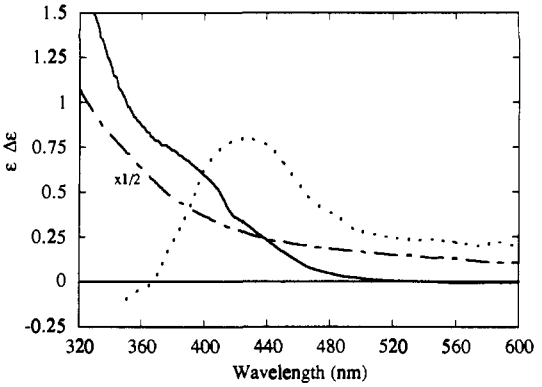

Figure 3. Charge-transfer spectral region of native Fe(+3)SBL. Room temperature optical absorption (---), CD (---), and LT MCD (—) spectra. The low-temperature MCD spectrum was recorded at 9.3 K and 6.0 T.

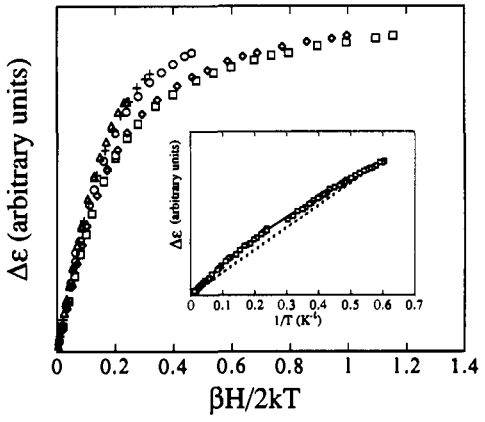

Figure 4. Magnetization saturation behavior for native Fe(3+)SBL. MCD intensity at 342 nm for a range of applied magnetic field strengths (0–5.9 T) at 1.7 K (□), 1.9 K (◇), 4.2 K (○), 6.2 K (+), and 8.4 K (△). Inset shows the temperature dependence of the MCD spectrum of native Fe(+3)SBL. Intensity (□) at 342 nm and 0.5 T. Curves represent fits obtained with eq 2 for the population of three doublets separated by 3.0 and 6.0 cm^{-1} with $C_1 = 2.22$, $C_2 = 4.6$, and $C_3 = 4.6$ (—) and for the ideal Curie behavior for an isolated doublet (---).

spectral region and are included in Figure 2. Tetrahedral[8a] $[FeCl_4]^-$ shows a negative band at 13800 cm^{-1} and a positive band at 16300 cm^{-1} (Figure 2B). Two positive bands in this spectral region are observed for the five-coordinate trigonal-bipyramidal[25] $[Fe(N_3)_5]^{2-}$ complex at 14000 and 16100 cm^{-1} (Figure 2C). Distorted octahedral[31] $[Fe(OX)_3]^{3-}$ has two main features: a positive band at 11400 cm^{-1} and a negative band[32] at 14700 cm^{-1} (Figure 2D). Seven-coordinate[23] $[FeEDTA{\cdot}H_2O]^-$ shows two positive features centered at 11800 and 16700 cm^{-1}, respectively (Figure 2E).

(iii) Charge-Transfer Region. Figure 3 gives the UV–vis, CD, and MCD spectra of Fe(+3)SBL in the 330–500-nm Fe(+3) CT region. Both the absorption and the CD spectra are in agreement with the literature[1a] and show a feature near 350 nm. In the MCD spectrum, there is an intense positive feature which starts as ~420 nm, associated with the 350-nm endogenous ligand-to-Fe^{3+} charge-transfer (CT) transition. A band due to a small amount (<1%) of heme contaminant is present in the MCD spectrum at 410 nm and is indicated by an asterisk.

Saturation magnetization data on the MCD intensity at 342 nm have been obtained at a series of temperatures and magnetic fields and are plotted in Figure 4 against the reduced energy parameter $\beta H/2kT$, where H is the strength of the applied magnetic field, T is the temperature, and β and k are the Bohr magneton and Boltzmann constant, respectively. As shown in

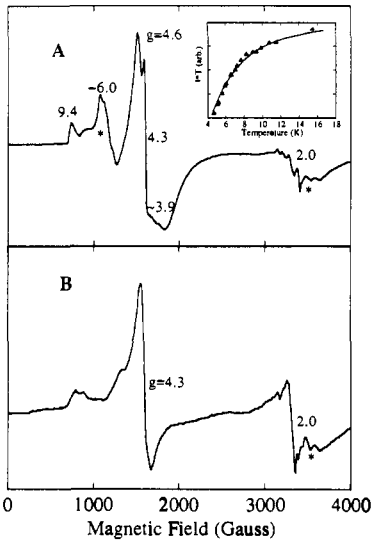

Figure 5. (Top) EPR spectrum of 0.87 mM Fe(+3)SBL–OCN^- at 4.5 K. The asterisks indicate the uncomplexed Fe(+3)SBL signal at $g \sim 6$ and Mn impurity in the $g \sim 2$ region. EPR parameters: microwave frequency, 9.513 GHz; power, 5 mW; modulation amplitude, 16 G. Inset shows the temperature dependence of the $g = 4.6$ EPR signal intensity. The EPR parameters used are the same as above. The EPR intensities were measured by the amplitudes of the $g = 4.6$ signal. Fit (—) obtained for population of three doublets equally separated by 4.7 cm^{-1}. (Bottom) EPR spectrum of 1.83 mM Fe(3+)SBL–N_3^- at 11.5 K. EPR parameters: microwave frequency, 9.513 GHz; power, 7.1 mW; modulation amplitude, 10 G.

Figure 4, the curves obtained at different temperatures do not superimpose. This nesting behavior is expected for a $S = {}^5/_2$ ferric site and is associated with the zero-field splitting of the ground state.[33] This nesting occurs because of thermal population of the higher energy Kramers doublets ($\pm{}^3/_2, \pm{}^5/_2$).

The temperature dependence of the MCD intensity of the 342-nm charge-transfer transition at a magnetic field of 0.5 T is presented in the inset in Figure 4. As can be seen from the data, the MCD intensity versus $1/T$ is not linear as would be expected for an isolated Kramers doublet (Curie law behavior). These data can be used to obtain an additional estimate of the ground-state zero-field splitting for ferric SBL as the deviations from linearity occur because of population of the higher M_S states. Thermal population of the ZFS $\pm M_S$ sublevels of the $S = {}^5/_2$ ground state gives the following expression for the C-term contribution to the MCD intensity at small applied fields:

$$\Delta\epsilon = \sum_{i=1}^{3} \frac{C_i}{kT} \alpha_i H \qquad (2)$$

where

$$\alpha_1 = \frac{1}{1 + e^{-2D/kT} + e^{-6D/kT}}$$

$$\alpha_2 = \frac{e^{-2D/kT}}{1 + e^{-2D/kT} + e^{-6D/kT}}$$

$$\alpha_3 = \frac{e^{-6D/kT}}{1 + e^{-2D/kT} + e^{-6D/kT}}$$

C_i is the C term intensity arising from each of the Kramers doublets, and α_i is the Boltzmann population weighting factor. Note that each Kramers doublet should also have a B-term contribution in eq 2 of the form $B_i\alpha_i H$ associated with field-induced mixing between doublets. We have estimated this contribution to be 1/25 of the total MCD intensity at the field of 0.5 T used in obtaining the data in Figure 4 and it can be neglected here.[34]

(31) Herpin, P. P. *Bull. Soc. Fr. Minéral. Cristallogr.* **1958**, *81*, 245.
(32) The negative band to lower energy corresponds to the ^4E component of the $^4T_1$.

(33) (a) Thomson, A. J.; Johnson, M. K. *Biochem. J.* **1980**, *191*, 411. (b) Johnson, M. K.; Robinson, A. E.; Thomson, A. J. In *Iron Sulfur Proteins*; Spiro, T. G., Ed.; Wiley: New York, 1979; pp 367–406.

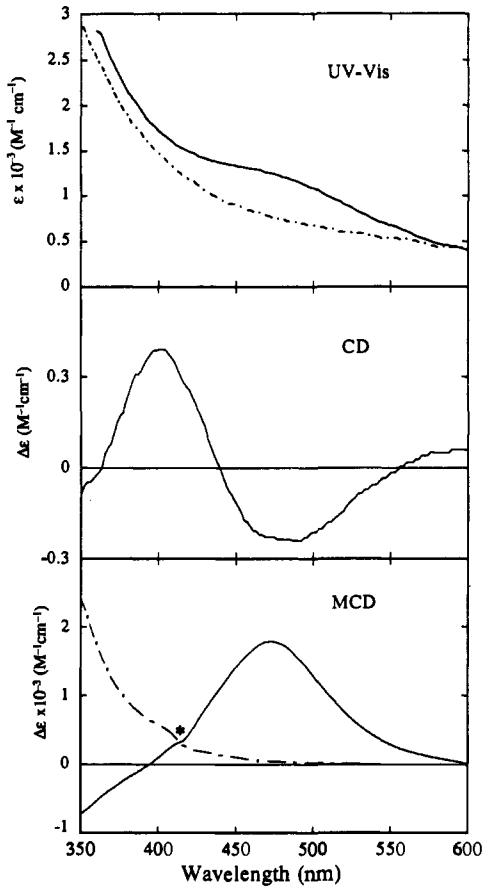

Figure 6. Anion binding to Fe(+3)SBL. Room temperature optical absorption (top), CD (middle), and low-temperature MCD (bottom) spectra for OCN^- (-·-) and N_3^- (—), respectively. The asterisk indicates a contribution from heme impurity. Low-temperature MCD spectra were recorded at 4.2 K and 3 T.

Using eq 2 to fit (solid line of Figure 4 inset) the experimental data (minimizing the sum of the square of the differences between data and fit) gives $D = 1.5 \pm 0.5$ cm^{-1} in agreement with the value derived from the temperature dependence of the EPR intensity (Table I).

B. Fe(3+)SBL–Exogenous Ligand Complexes. (i) EPR. Upon addition of either N_3^- or OCN^- to Fe(3+)SBL, the EPR spectrum is found to change dramatically (Figure 5). New peaks appear in the spectrum at $g = 4.6$ (strong) and 9.4 (weak) for the OCN^- complex and at $g = 4.3$ for the N_3^- bound form. The axial Fe(+3)SBL signal at $g_\perp \sim 6$ is found to decrease concomitantly with the appearance of these features, indicating that the new features are arising due to a perturbation of the Fe(+3) center associated with ligand addition. From these observed g values, E/D ratios of 0.27 and 0.33 are found for Fe(+3)SBL–OCN^- and Fe(+3)SBL–N_3^-, respectively. Therefore, interactions with N_3^- and OCN^- cause the coordination environment of Fe(+3)SBL to go from axial to rhombic. For a rhombic system, the three ground-state doublets are equally spaced by an amount $Z = 3.5D$ which can be obtained from the temperature dependence of the intensity of the rhombic $g = 4.6$ EPR signal associated with the middle doublet of Fe(+3)SBL–OCN^- (Figure 5 inset) and is determined to be 4.7 ± 1 cm^{-1} ($D = 1.3 \pm 1$ cm^{-1}). Inserting these spin Hamiltonian parameters into eq 1 gives g values of 9.44, 0.88, and 1.36 for the lowest doublet. These results are included in Table I.

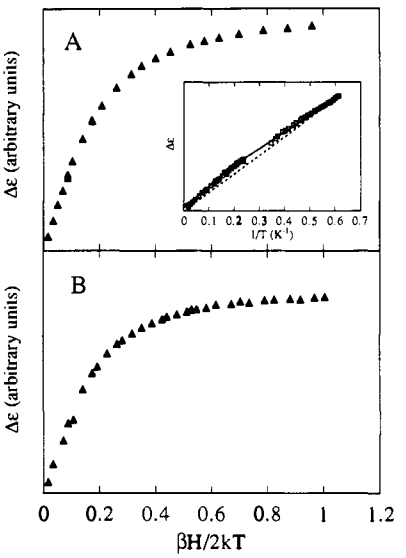

Figure 7. Magnetization saturation behavior at the CT region for anion-bound forms of Fe(+3)SBL. (Top) MCD amplitude at 342 nm for a range of applied magnetic field strengths (0–5.9 T) at 1.9 K for Fe(+3)SBL–OCN^-. Inset shows the temperature dependence of the MCD spectrum of Fe(+3)SBL–OCN^-. Intensity (□) at 342 nm and 0.5 T for the Fe(+3)SBL–OCN^- complex. Curves represent fits obtained with eq 3 for population of three doublets separated by 4.0 and 8.0 cm^{-1} (—) with $C_1 = 2.5$, $C_2 = 4.5$, and $C_3 = 4.5$ and for the ideal Curie behavior for an isolated doublet (---). (Bottom) MCD amplitude at 470 nm for a range of applied magnetic field (0–5.9 T) at 1.9 K for Fe(+3)SBL–N_3^-.

(ii) Charge-Transfer Region. Upon adding N_3^- a new intense 470-nm ($\epsilon = 1.7 \times 10^3$) band appears in the Fe(+3)SBL–N_3^- spectra (Figure 6) which is assigned as an $N_3^- \rightarrow$ Fe(+3) CT transition, demonstrating that the azide binds directly to the Fe(+3) site. In contrast, addition of OCN^- does not lead to any observable change in the 350–500-nm region relative to native Fe(+3)SBL. Thus, no $OCN^- \rightarrow$ Fe(+3) CT transition contributes in this spectral region.

However, as indicated by the EPR spectra in Figure 5, N_3^- and OCN^- perturb the EPR spectrum of Fe(+3)SBL in a very similar way, suggesting that OCN^- interacts with the Fe(+3) in a manner which parallels N_3^- coordination. The VT MCD data of the 342-nm band in the Fe(+3)SBL–OCN^- complex (Figure 7A inset) were used to obtain an additional estimate of the ground-state zero-field splitting of the rhombic system with eq 3.

$$\Delta\epsilon = \sum_{i=1}^{3} \frac{C_i}{kT} \alpha_i H \qquad (3)$$

where

$$\alpha_1 = \frac{1}{1 + e^{-Z/kT} + e^{-2Z/kT}}$$

$$\alpha_2 = \frac{e^{-Z/kT}}{1 + e^{-Z/kT} + e^{-2Z/kT}}$$

$$\alpha_3 = \frac{e^{-2Z/kT}}{1 + e^{-Z/kT} + e^{-2Z/kT}}$$

A value of Z of 4 ± 1 cm^{-1} is obtained. Again this is consistent with the value estimated from EPR (Table I). As for the Fe(+3)-SBL case, B-term contributions to eq 3 are estimated to be 1/20 of the total intensity at 0.5 T and can be neglected.[34]

The saturation magnetization data on Fe(+3)SBL–N_3^- and Fe(+3)SBL–OCN^- complexes were obtained at low temperature (2 K) with the 470-nm ($N_3^- \rightarrow$ Fe(+3) CT) and 342-nm (en-

(34) This estimate of the B-term contribution was obtained by a least-squares linear fitting of the high-field saturation data in Figures 4 and 7a at lowest temperature. The slope obtained is the coefficient for the field-dependent B term. The B-term intensity was calculated from this slope and compared with the experimental data at $H = 0.5$ T. This calculated B term is appropriate for the lowest doublet (B_1) and therefore was applied to fit the low-temperature limit of the MCD temperature-dependent data in the inset. For the high-temperature limit, all three Kramer's doublets are equally populated and the total B-term intensity contribution is zero as the B_i's are equal in magnitude but opposite in sign. A B-term contribution due to the higher doublets could affect the fit at intermediate temperatures; however, this has to be more than an order of magnitude larger than the B term obtained for the lower doublet, which is unlikely and not consistent with the ZFS value obtained by using only C terms (eqs 2 and 3) which is in agreement with the ZFS value obtained from EPR data.

dogenous ligand → Fe(+3) CT) bands respectively and are presented in Figure 7.

Analysis

A. Native Fe(+3)-SBL. (i) Ligand-Field Transitions. All the d → d transitions of mononuclear high-spin Fe(+3) are spin forbidden, and therefore have very low extinction coefficients ($\epsilon \leq 1\ M^{-1}\ cm^{-1}$), and are not detectable by absorption spectroscopy at accessible protein concentrations (mM). However, these transitions can be seen in the low-temperature ($T = 4$ K) MCD spectra of Fe(3+)SBL (Figure 2). These d → d transitions are of interest as their energies are sensitive to the geometry and bonding interactions of the Fe(+3) site and thus can be used to probe the active site structure. In addition, the sign of an MCD feature arising from a given $^6A_1 \rightarrow {}^4\Gamma$ transition is dependent on the approximate site symmetry of the Fe(+3) center and thus gives added information concerning site geometry. To explore such correlations, the experimental and theoretical results of MCD C-term signs and $^6A_1 \rightarrow {}^4\Gamma$ transition energies were investigated for a series of high-spin ferric model complexes with different geometries.

Because the LF transitions are spin forbidden they gain absorption intensity through spin–orbit coupling with spin-allowed transitions. This mechanism involves spin–orbit coupling of $^4T_1$ LF excited-state character into the $^6A_1$ ground state and spin–orbit coupling of $^6T_2$ charge-transfer excited-state character into the $^4\Gamma$ LF state, and can be described by eq 4A

$$\langle {}^6A_1 M_S|M_q|{}^4\Gamma h M_S'\rangle = \frac{\langle {}^6A_1 M_S|H_{so}|{}^4T_1 h' M_S'\rangle\langle {}^4T_1 h' M_S'|M_q|{}^4\Gamma h M_S'\rangle}{(E({}^4T_1) - E({}^6A_1))} + \frac{\langle {}^6A_1 M_S|M_q|{}^6T_2 h'' M_S\rangle\langle {}^6T_2 h' M_S|H_{so}|{}^4\Gamma h M_S'\rangle}{(E({}^6T_2) - E({}^4\Gamma))} \quad (4A)$$

where M_S and M_S' are the spin components of the $^6A_1$ and $^4\Gamma$ states; h, h', and h'' are the orbital components of the $^4\Gamma$, $^4T_1$, and $^6T_2$ states; M_q is the electric dipole operator; and H_{so} is the spin–orbit operator. This mechanism also leads to MCD C-term activity and can be used to predict the MCD signs associated with each of the LF features. The sign of an MCD feature is given by eq 4B

$$C_0 = -\frac{1}{|A|}\sum_{\substack{\alpha\lambda \\ \alpha'\lambda'}} \langle A\alpha'|(L_Z + 2S_Z)|A\alpha\rangle[\langle A\alpha|m_{-1}|J\lambda\rangle \times \langle A\alpha'|m_{-1}|J\lambda'\rangle^* - \langle A\alpha|m_{+1}|J\lambda\rangle\langle A\alpha'|m_{+1}|J\lambda'\rangle^*] \quad (4B)$$

where $(L_Z + 2S_Z)$ is the Zeeman operator; $m_{\pm 1}$ is the electric dipole operator for the absorption of right (+) and left (−) circular polarized light; α, α', λ, and λ' are the components of the ground (A) and excited (J) states; and $|A|$ is the ground-state degeneracy ($|A| = 6$).

On the basis of LF theory, the two lowest energy d → d transitions for a high-spin ferric site with cubic symmetry are the $^6A_1 \rightarrow {}^4T_1$ and $^6A_1 \rightarrow {}^4T_2$ transitions, with the $^6A_1 \rightarrow {}^4T_1$ at lower energy. Typically these two bands are the only transitions that can be observed without interference from the intense spin-allowed ligand → metal charge-transfer transitions, and thus the following analysis will focus on these transitions.

Equations 4A and 4B allow a prediction of the sign of the MCD feature associated with a given $^6A_1 \rightarrow {}^4T_1$ or $^6A_1 \rightarrow {}^4T_2$ transition. The sign of a C term is dependent on the symmetry of the site, and thus the predicted signs have been determined for three geometries (T_d, C_{4v} (square pyramidal), and D_3 distorted O_h) and are given in Table II. For the T_d and D_3 model complexes the predicted C-term sign is consistent with the observed MCD spectra in Figure 2. In addition to the theoretically predicted signs, experimentally observed MCD features associated with the LF transitions in a trigonal-bipyramidal $[Fe(N_3)_5]^{2-}$ and a seven-coordinate $[FeEDTA{\cdot}H_2O]^-$ complex are also included in Table II.

A negative C term is observed in the LF region of the MCD spectrum of native Fe(+3) SBL at 13 300 cm^{-1} (Figure 2A). The negative sign of the MCD can be used to immediately rule out the five-coordinate trigonal-bipyramidal and seven-coordinate pentagonal-bipyramidal geometries for the Fe(+3) coordination environment. This leaves four-coordinate T_d ($^6A_1 \rightarrow {}^4T_1$), five-coordinate square-pyramidal ($^6A_1 \rightarrow {}^4T_2$), and six-coordinate distorted-octahedral ($^6A_1 \rightarrow {}^4T_2$) coordination environments as possibilities. However, since the ferrous SBL active site is six coordinate,[4] it is very unlikely that the oxidation from Fe(+2) to Fe(+3) can result in the loss of two ligands. This conclusion is supported by XANES studies on ferric SBL which indicate the presence of 6 or 7 ligands.[20] Therefore, the 13 300-cm^{-1} negative MCD band cannot be due to the $^6A_1 \rightarrow {}^4T_1$ transition in a T_d site and must be the $^6A_1 \rightarrow {}^4T_2$ transition in a square-pyramidal or six-coordinate geometry.

Table II

CN	symmetry	$^4T_1$ C-term sign	$^4T_1$ energy,[a] cm^{-1}	$^4T_2$ C-term sign	$^4T_2$ energy,[a] cm^{-1}
4	tetrahedral	(−)	16500–18100	(+)	19900–20900
5	trigonal bipyramidal	(+)	14000[b]	(+)	16100[b]
5	square pyramidal	(+)	7500–11000	(−)	17100–20100
6	distorted octahedral	(+)	7200–11400	(−)	12000–15800
7	pentagonal bipyramidal	(+)	11800[c]	(+)	16700[c]

[a] Ranges based on data and ligand-field theory. [b] Data on $[Fe(N_3)_5]^{2-}$. [c] Data on $[FeEDTA{\cdot}H_2O]^-$.

Ligand-field considerations eliminate the five-coordinate square-pyramidal geometry. The values of the electron-repulsion parameters, B and C, for a high-spin ferric site with six biologically relevant O and N ligands can be reasonably estimated to be 690 and 3050 cm^{-1}, respectively.[35a] The coordination of six amine ligands leads to a Dq value[35b] of 1700–1800 cm^{-1}. This value represents an upper limit of Dq as typical biologically relevant ligands have ligand field strengths less than or equal to amine. Using the estimated Racah parameters and Dq in the Tanabe–Sugano matrices[36] gives $E(^4T_2) \approx$ 11500–12500 cm^{-1}. This is a lower limit for $E(^4T_2)$ as smaller values of Dq increase $E(^4T_2)$. Removal of an axial ligand reduces the Dq value by about one-sixth, giving $E(^4T_2(av)) \approx$ 14000–15000 cm^{-1}, where $^4T_2(av)$ is the degeneracy weighted average energy of the $^4T_2$ orbital components. The removal of a ligand also splits the $^4T_2$ state, producing $^4B_2(^4T_2(0))$ and $^4E(^4T_2(\pm 1))$ orbital states due to stabilization of the d_{z^2} relative to the $d_{x^2-y^2}$ orbital. This causes the $^4T_2(0)$ state to move to higher energy while the $^4T_2(\pm 1)$ shifts to lower energy. The low symmetry splitting of the $^4T_2$ state is given by the equation[37]

$$\Delta^4T_2 = (3/4)\mu \quad (5)$$

where $\Delta^4T_2 = (E(^4T_2(0)) - E(^4T_2(\pm 1)))$, and $\mu = (E(d_{x^2-y^2}) - E(d_z))$. The energy of the $E(^4T_2(0))$ is $E(^4T_2(av)) + (^2/_3)(\Delta^4T_2) = E(^4T_2(av)) + (^1/_2)(E(d_{x^2-y^2}) - E(d_z))$. μ is ≥5000 cm^{-1} as estimated from the splitting of the $d_{x^2-y^2}$ and d_{z^2} orbitals observed in five-coordinate C_{4v} Fe(+2) complexes.[4] These parameters give a lower limit[38] for $E(^4T_2(0))$ of 16500–17500 cm^{-1}. This underestimates the energy of this transition in a square-pyramidal complex as the $d_{x^2-y^2}$ and d_{z^2} splitting is likely to be larger in ferric complexes for the same ligands. As the $^4T_2(0)$ is the MCD active component of the $^4T_2$ state, removal of a ligand from a six-coordinate site causes the negative MCD band from the $^4T_2$ to move

(35) (a) The B and C values were estimated from an average of these parameters obtained from a ligand-field analysis of the observed d → d transitions in a series of six model complexes with O and N ligands (Fatta, A.; Lintvedt, R. *Inorg. Chem.* **1972**, *11*, 88. Lehmann, G. *Z. Phys. Chem. Neue Folge* **1970**, *72*, 279. Bernas, H.; Langevin, M. *J. Phys.* **1963**, *24*, 1034. Garbett, K.; Lang, G.; Williams, R. J. P. *J. Chem. Soc.* **1971**, 3433. Holt, S.; Dingle, R. *Acta Chem. Scand.* **1968**, *22*, 1091). (b) The estimate of Dq was obtained by using the f and g parameters of Jørgensen (Jørgensen, C. K. *Oxidation Numbers and Oxidation States*; Springer: New York, 1969; pp 84 and 85).

(36) Sugano, S.; Tanabe, Y.; Kamimura, H. *Multiplets of Transition-Metal Ions in Crystals*; Academic: New York, 1970.

(37) Goode, D. H. *J. Chem. Phys.* **1965**, *43*, 2830.

(38) For a five-coordinate complex with three amine ligands and two H_2O ligands Dq ≈ 1360 cm^{-1}, thus placing the negative MCD feature $^4T_2(0)$ at ≈16 500 cm^{-1}.

from 11500–12500 to 16500–17500 cm^{-1}. Thus, the negative MCD band at 13 300 cm^{-1} in Fe(+3)SBL is most reasonably assigned as the $^6A_1 \rightarrow {}^4T_2$ transition for a distorted octahedral active site. Therefore the Fe(+2)SBL active site remains six coordinate upon oxidation to Fe(+3)SBL.[39]

(ii) VTVH MCD. Schatz et al.[12] have demonstrated that for a randomly oriented (e.g. frozen solution) absorbing species with axial symmetry and an isolated Kramers doublet ground state (i.e. $S = {}^1/_2$), the MCD intensity is described[14] by eq 6. Unlike the MCD expressions used in the linear limit, this expression is valid at all values of $\beta H/2kT$, and thus can be used to describe the saturation behavior of the MCD signal. In eq 6, $\Gamma = ((\sin^2\theta)g_\perp{}^2 + (\cos^2\theta)g_\parallel{}^2)^{1/2}$, θ is the angle between the magnetic field vector

$$\frac{\Delta\epsilon}{K} = M_{xy}{}^2\left\{\int_0^{\pi/2}\frac{\cos^2\theta\sin\theta}{\Gamma}g_\parallel\tanh\left(\frac{\Gamma\beta H}{2kT}\right)d\theta - \sqrt{2}\frac{M_z}{M_{xy}}\int_0^{\pi/2}\frac{\sin^3\theta}{\Gamma}g_\perp\tanh\left(\frac{\Gamma\beta H}{2kT}\right)d\theta\right\} \quad (6)$$

and the molecular z axis, M_z and $M_{x,y}$ are the transition dipole moments along molecular z and x,y axes, and K is a constant. The first term of the equation takes into account the contributions to the MCD intensity from x,y-polarized absorption, while the second term accounts for the z-polarized absorption. The integration in eq 6 is over all possible orientations of the molecules. The integrals in eq 6 cannot be solved analytically; however, the MCD intensity can be determined numerically at each value of $\beta H/2kT$.

As has been pointed out by Bennett and Johnson,[14] if the g values associated with the ground-state Kramers doublet are known (i.e. from EPR), then eq 6 can be used to obtain polarization ratios for the MCD active transition. This allows polarization information to be obtained for randomly oriented molecules in a frozen solution. This is useful when applied to CT features in a low-symmetry complex because the CT transition will be dominantly polarized along the ligand–metal bond and thus the polarization can be used to obtain structural information concerning the orientation of the ligands relative to the principal directions of the **g** tensor of the lowest doublet. In high-spin ferric complexes, the g value coordinate system is collinear with the ZFS tensor coordinate system, and thus the polarization information obtained in this type of analysis is relative to the coordinate system which diagonalizes the ZFS tensor.

Because of the axial nature of the native Fe(+3)SBL ground state (Table I) this type of treatment is particularly appropriate for analysis of the polarization of its 350-nm CT transition. Fe(+3)SBL has a positive D and thus the $M_S = \pm{}^1/_2$ Kramers doublet is lowest, with the $M_S = \pm{}^3/_2$ and $\pm{}^5/_2$ at 3.0 and 9.0 cm^{-1} respectively. At low temperatures ($T \approx 1.7$ K), only the $M_S = \pm{}^1/_2$ doublet is significantly populated, and eq 6 can be used to obtain the M_z/M_{xy} polarization ratio. Equation 6 was evaluated by numerical integration by using the g values of $g_z = 2.0$ and $g_{xy} = 6.0$ associated with the $M_S = \pm{}^1/_2$ doublet. A set of saturation magnetization curves were calculated for different M_z/M_{xy} polarization ratios and compared with the experimental 1.7 K saturation data for the 350-nm CT transition which was normalized to the best fit saturation limit (Figure 8A). The best fit to the data requires the transition to be strongly x,y polarized. However, there is clearly some deviation between the experimental data and the calculated curve. This deviation could derive from either of two mechanisms: B terms (i.e. a field-induced mixing of sublevels in the ground state) which can only occur for non-x,y-polarized transitions or population of the higher energy doublets of the ground state which does in fact occur for x,y-polarized transitions in native Fe(+3)SBL at 1.7 K (vide infra). To evaluate the B-term possibility, the high-field portion of the saturation magnetization data in Figure 8A has been used to obtain a B-term contribution which is linear in field. The slope obtained is subtracted from the data to generate the plot in Figure 8B (squares). As can be seen, the B-term-corrected data lie within the curves generated with polarization ratios of $0 \rightarrow 0.5$, indicating that the 350-nm transition is a minimum of 66% x,y polarized. However, this $\geq$66% x,y polarized component will contribute to the field dependence of the experimental 1.7 K saturation data in Figure 8A at high field (vide infra), and subtracting this contribution from the experimental data in Figure 8A gives the solid diamonds in Figure 8B and a polarization ratio for the best fit of 0 (Figure 8B, solid diamond). Therefore, the deviation in Figure 8A between the calculated $M_z/M_{xy} = 0$ curve and the experimental data occurs because of population of the higher doublets which becomes significant at $\beta H/2kT > 0.3$ ($H > 2.5$ T at 1.7 K). When the ZFS parameters of Table I are used, the magnetic field splits each doublet as plotted in Figure 9. As can be seen from the figure, for a field along z, the $M_S = -{}^3/_2$ sublevel crosses the $M_S = -{}^1/_2$ sublevel at $H \sim 2.5$ T, while the $M_S = -{}^5/_2$ crosses at $H \sim 4.5$ T. When H is applied perpendicular to molecular z axis, there is no crossing between sublevels. Since a significant portion of the population resides in the two higher

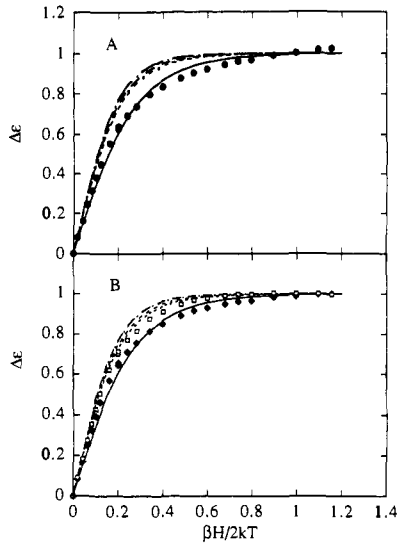

Figure 8. (Top) Fit of the experimental magnetization data of native Fe(+3)SBL at 1.7 K with eq 6 ($M_{xy} = 1$). Curves show the effect of changing the polarization ratio, $P = |M_z/M_{xy}|$, from 0 to −100 (p = 0 (—), 0.5 (···), 1.0 (- - -), 10 (-·-), 100 (- -)). (Bottom) B-term corrected magnetization plots (see text for details).

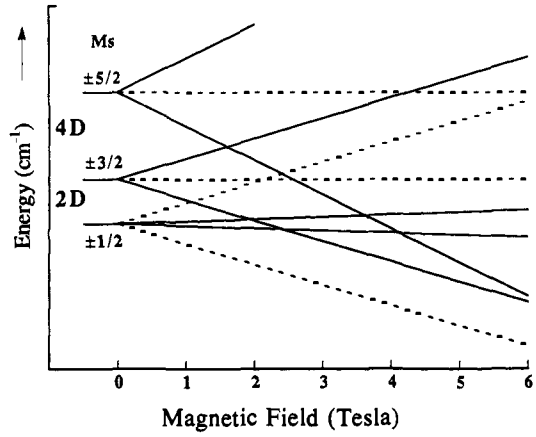

Figure 9. Zeeman splitting of the $S = {}^5/_2$ energy levels for an axial ferric site with $D = 1.5$ cm^{-1} for H parallel to z (—) and H parallel to x,y (- - -).

(39) To perform this analysis, one must consider a reasonable level of symmetry. However, when the symmetry is lowered (as in a protein active site), all the information content is not lost except in extreme situations. In particular, for a six-coordinate Fe(+3) complex, the predicted sign of the MCD C term for the $^4T_2$ transition remains the same whether the complex is trigonally or tetragonally distorted. Application of both distortions simultaneously to a six-coordinate complex to induce lower symmetry still results in a negative C term for the $^4T_2$ transition. Further, six model complexes with mixed N and O ligation and different extents of distortion from octahedral have been used to estimate the energy range for the $^4T_2$ transition listed in Table II.

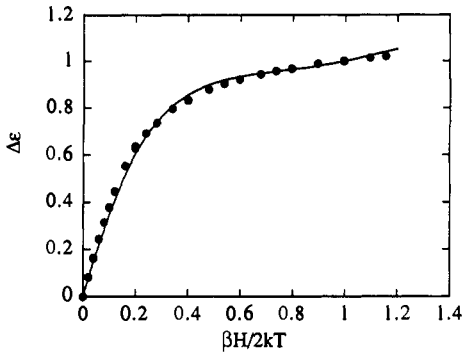

Figure 10. Best fit (—) of eq 7 to the Fe(+3)SBL magnetization data (●) with $a_1 = 1$, $a_2 = 0.35$, $a_3 = 0.45$, $M_z/M_{xy} = 0$, and $M_{xy} = 1$.

doublets at fields above 2 T, the assumption of an isolated $M_S = \pm^1/_2$ doublet is no longer valid and contributions from all 3 doublets must be taken into account. Since the transition in Fe(+3)SBL is found to be x,y polarized for the ground doublet, and since the transitions from all three doublets will have the same M_z/M_{xy} ratio, the second term in eq 6 can be neglected. The total MCD intensity ($\Delta\epsilon_{total}$) is the sum of the contributions from each doublet weighted by its Boltzmann population at each $\beta H/2kT$ value and is given by eq7.

$$\Delta\epsilon_{Total} = \sum_{i=1}^{3}(a_i\Delta\epsilon_i\alpha_i) \qquad (7)$$

The sum, i, is over the three doublets, $\Delta\epsilon_i$, is the MCD intensity from the ith doublet calculated with eq 6, α_i is the fractional population of the ith doublet, and a_i is an intensity weighing factor for each doublet. Using eq 7 and adjusting the a_i parameters to obtain the best fit gives the calculated saturation magnetization curve which is compared to the experimental data in Figure 10. The population weighted magnetic saturation curve matches the experimental data quite well in both the low- and high-field regions with no need for additional B-term contributions.

The x,y-polarization nature of the 342-nm CT transition from Fe(+3)SBL indicates that the chromophoric ligand(s) must be in the xy plane of the iron site, as defined by the **g** tensor coordinate system. On the basis of EXAFS studies which indicate the presence of 4 ± 1 imidazoles for the ferrous site and the fact that both SOD and half-met hemerythrin are known to have bound histidine and exhibit a transition at ~350 nm which is likely a his → Fe(+3) CT transition, the dominant contribution to the 350-nm band in Fe(+3)SBL can reasonably be assigned as his → Fe(+3) CT transitions. C-term MCD intensity requires two perpendicular transition moments, which are determined to be in the x and y equatorial directions for the 350-nm band. These transition moments can come from either two degenerate (at 350 nm) or nondegenerate CT states; the latter possibility would derive from spin–orbit mixing of a higher energy state into the 350-nm transition. We strongly favor the former mechanism as EXAFS data[18] indicate that at least three imidazoles are present and thus contribute to the 350-nm transition. From the MCD analysis, these bind along only the x and y directions, which is further supported by the ZFS analysis (vide infra) which requires the presence of strong field ligands (i.e. histidine) in the equatorial plane.

B. Exogenous Ligand Binding. (i) Fe(+3)SBL–OCN^- Complex. From Figure 5, the EPR signal becomes rhombic when OCN^- is added to native Fe(+3)SBL, indicating that, as with N_3^-, OCN^- binds to the Fe(+3) site, and coordination of the exogenous ligand has significantly changed the electronic and geometric structure. No new CT feature is observed in the absorption spectrum upon OCN^- binding. As the endogenous 350-nm his → Fe(+3) CT band can still be observed in the OCN^- bound form, this transition provides a useful reference for an analysis of the active site perturbations associated with exogenous ligand binding. An analysis of the polarization of the 350-nm band has been performed to determine whether this transition remains x,y polarized in the

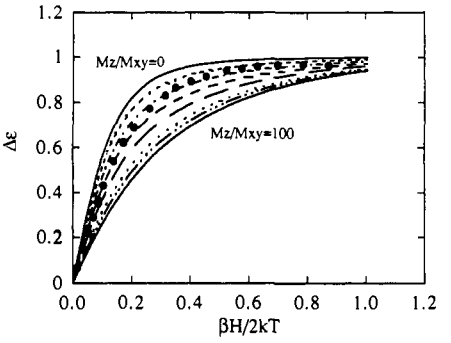

Figure 11. Fit of eq 6 to B-term-corrected magnetization saturation data at 1.9 K for Fe(+3)SBL–OCN^- ($M_{xy} = 1$). Solid curves represent predicted magnetization saturation behavior as a function of increasing polarization ratio M_z/M_{xy}. (Starting from the top curve $|M_z/M_{xy}| = 0$, 0.2, 0.5, 1, 2, 5, 10, and 100.)

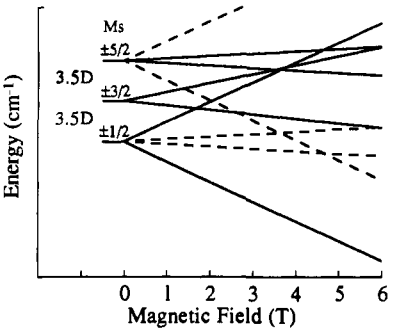

Figure 12. Zeeman splitting of $S = {}^5/_2$ energy levels for a rhombic ferric site with $D = 1.1$ cm^{-1}, $E/D = 0.27$ for H parallel to z (—) and H parallel to xy (--). Here z is defined as the $g = 9.44$ direction of the lowest doublet.

coordinate system defined by the **g** tensor of the Fe(+3)SBL–OCN^-.

For this rhombic high-spin Fe(+3) site, the lowest doublet has g values of 0.88, 1.36, and 9.44 (Table I). While only one EPR signal for this ground doublet is observed, the other two can be calculated from the observed D and E/D. Following a similar treatment by Bennett and Johnson,[14] this can be treated as an effective axial system by averaging the two small g values as $g_\perp$ and defining the unique $g = 9.44$ as $g_\parallel$. It should be noted that an inherent assumption made in this treatment is that the orientation of the **g** tensor coordinate system and the polarizations of the transitions are collinear; however, as will be shown below, this is not always the case.

With use of eq 6, with $g_\parallel = 9.44$ and $g_\perp = ((g_2^2 + g_3^2)/2)^{1/2} = 1.15$ for the Fe(+3)SBL–OCN^- complex, the MCD intensity was calculated as a function of $\beta H/2kT$ for a series M_z/M_{xy} values, and a series of saturation magnetization curves were generated as given in Figure 11. As described for the native Fe(+3)SBL, the experimental data for Fe(+3)SBL–OCN^- in Figure 7A are corrected for a B-term contribution from the slope of the high-field region. The resulting saturation magnetization plot is also included in Figure 11 (circles). As can be seen from this figure, none of the calculated curves can account for the observed data points. As for the analysis of native Fe(+3)SBL, the validity of the isolated doublet assumption was examined. The experimental Z and the g values (in Table I) give the energies of the doublets as a function of the field applied parallel and perpendicular to $g_\parallel = 9.44$ (Figure 12). Under the experimental conditions, it is observed that, except in the perpendicular field orientation at $H > 5T$, there is no crossing of the upper doublet levels with the lowest sublevel. Therefore, population of the upper doublets is not significant and cannot account for the poor agreement between the data and the calculated curves.

As mentioned above, upon binding OCN^- the axial native EPR signal becomes rhombic. Therefore the requirement that the **g** tensor lies along the original polarizations of the bands is relaxed,

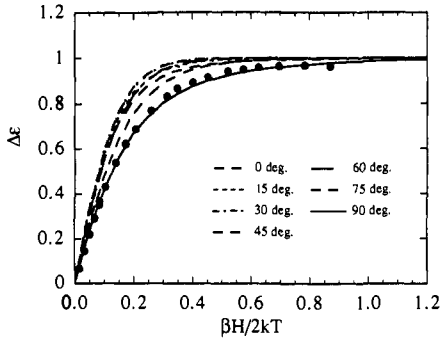

Figure 13. Calculated saturation magnetization curves for the Fe(+3)-SBL–OCN^- at 1.9 K as a function of α (see text for details).

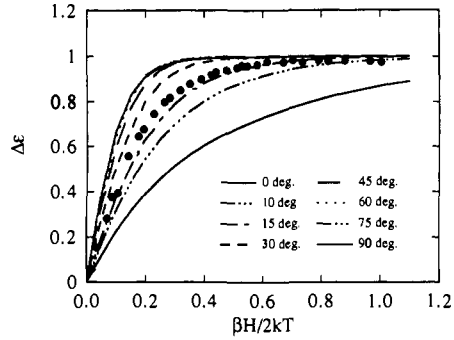

Figure 14. Calculated saturation magnetization curves for Fe(+3)SBL–N_3^- at 1.9 K as a function of α (see text for details).

and thus the **g** tensor can rotate off the original coordinate system by an angle α. Since we have determined that the 350-nm band is x,y polarized in native Fe(+3)SBL, it is expected to remain x,y polarized in the native coordinate system upon OCN^- binding. This transition moment coordinate system is then used as a reference. The MCD data can then be described by eq 6, with the modification that the **g** tensor coordinate system is rotated into the coordinate system defined by the x,y-polarized transition. Thus the g values observed in the EPR will be related to the MCD effective g values through the direction cosines for the rotation. Approximating the g values of the lowest doublet as 9.44, 1.15, 1.15, then

$$g_\parallel' = \sqrt{9.44^2 \cos \alpha^2 + 1.15^2 \sin \alpha^2}$$

$$g_\perp' = \sqrt{9.44^2 \sin \alpha^2 + 1.15^2 \cos \alpha^2}$$

where the primed g values are those in the MCD coordinate system and the angle α is that between the $g = 9.44$ direction and the direction perpendicular to the x,y-polarized transition. Only the first term in eq 6 (i.e. the x,y-polarization term) is necessary and it is found that an angle α of 90° is required to explain the B-term-corrected MCD data (Figure 13). Thus the unique $g = 9.44$ direction for Fe(+3)SBL–OCN^- is 90° away from the original z axis of the native Fe(+3)SBL and lies in the x,y plane. The $g = 9.44$ corresponds to g_y in the native coordinate system, and this indicates that the ZFS tensor retains its original orientation upon going rhombic with anion binding.

(ii) Fe(+3)SBL–N_3^- Complex. As for the Fe(+3)SBL–OCN^-, addition of N_3^- to the native protein causes the EPR signal to become rhombic, indicating a similar binding mode. In contrast to Fe(+3)SBL–OCN^-, an intense 470-nm $N_3^- \rightarrow$ Fe(+3) CT transition is present for Fe(+3)SBL–N_3^-. This feature obscures the endogenous 350-nm CT transition; however, a similar analysis has been performed on this exogenous L → Fe(+3) CT transition. As the polarization of this CT transition will be dominantly along the Fe–N_3^- bond, this information can be used to determine the orientation of this ligand relative to the **g** tensor coordinate system. Equation 6 was applied to the B-term-corrected saturation data to determine the polarization of the $N_3^- \rightarrow$ Fe(+3) CT transition, using the calculated g values of the ground doublet (9.67, 0.86, 0.61; Table I). As with Fe(+3)SBL–OCN^- it is found that a good fit cannot be obtained for any value of the polarization ratio, M_z/M_{xy}.

The $N_3^- \rightarrow$ Fe(+3) CT transition will be polarized along the N_3^-–Fe(+3) bond. In this limit there can be no MCD density, as MCD requires two perpendicular non-zero electric dipole transition moments. The fact that this CT transition exhibits a C-term MCD signal indicates that spin–orbit coupling is mixing in transition moments perpendicular to the direction of the $N_3^- \rightarrow$ Fe(+3) CT transition. The coordinate system is again chosen to be defined by the transition moments such that the $N_3^- \rightarrow$ Fe(+3) CT transition is along the z axis; then spin–orbit coupling is required to mix M_x and M_y intensity into this transition. The values of M_x and M_y should be at least an order of magnitude less than that of M_z. In addition, it is assumed that spin–orbit coupling is isotropic, thus $M_x \approx M_y$. Therefore, only the second term of eq 6 is required since $M_z M_{xy} \gg (M_{xy})^2$. As with the OCN^- case, the real g values are approximated as 9.67 and 0.75 and the effective g' values which determine the saturation behavior are

$$g_\parallel' = \sqrt{9.67^2 \cos \alpha^2 + 0.75^2 \sin \alpha^2}$$

$$g_\perp' = \sqrt{9.67^2 \sin \alpha^2 + 0.75^2 \cos \alpha^2}$$

where the angle α is now between the $g = 9.67$ direction and the Fe(+3)–N_3^- bond. By using this approach to fit the saturation magnetization data, which has been corrected for a B-term contribution from Figure 7B as described earlier, α is found to be ~15° (Figure 14). Thus, this analysis of the MCD data gives the orientation of the Fe(+3)–N_3^- bond relative to the $g_\parallel = 9.67$ direction.

From the Fe(+3)SBL–OCN^- analysis, $g = 9.44$ lies in the x,y plane of the native ferric enzyme. Since OCN^- and N_3^- perturb the Fe(+3)SBL spectrum in a similar way, it is reasonable to assume that there are no other significant structural perturbations and that the directions of the unique g value in the OCN^- and N_3^- complexes are the same. Therefore, the 15° angle between the Fe(+3)–N_3^- bond and the $g = 9.67$ value implies that N_3^- binds approximately in the x,y plane and likely replaces a ligand, which is consistent with the observation of H_2O or OH^- coordination in the native ferric SBL.[19]

C. Origin of the Ground-State Zero-Field Splitting. From Table I Fe(+3)SBL has an axial EPR signal with positive ZFS $D = +1.7 \pm 0.5$ cm^{-1} ($E/D = 0.01$), and upon ligand binding the EPR signal becomes rhombic ($E/D \approx 0.33$) but with no rotation of the **g** tensor (from the MCD analysis). To better understand the information content of the ZFS, we have considered its origin in terms of a ligand-field model.

Griffith[7] derived a model to account for the ferric $^6A_1$ ground-state ZFS through second-order spin-orbit coupling between the ground state and the low-lying $^4T_1$ ligand-field excited state, as given by eq 8, where D is the axial ZFS parameter of

$$D = \frac{1}{360}\left[\frac{2|\langle {}^6A_1||H_{so}||{}^4T_1(z)\rangle|^2}{E({}^4T_1(z))} - \frac{|\langle {}^6A_1||H_{so}||{}^4T_1(y)\rangle|^2}{E({}^4T_1(y))} - \frac{|\langle {}^6A_1||H_{so}||{}^4T_1(x)\rangle|^2}{E({}^4T_1(x))}\right] \quad (8A)$$

$$= \frac{(\zeta_{Fe^{3+}})^2}{10}\left[\frac{2}{E({}^4T_1(z))} - \frac{1}{E({}^4T_1(y))} - \frac{1}{E({}^4T_1(x))}\right] \quad (8B)$$

$$E = \frac{1}{360}\left[\frac{|\langle {}^6A_1||H_{so}||{}^4T_1(y)\rangle|^2}{E({}^4T_1(y))} - \frac{|\langle {}^6A_1||H_{so}||{}^4T_1(x)\rangle|^2}{E({}^4T_1(x))}\right] \quad (8C)$$

$$= \frac{(\zeta_{Fe^{3+}})^2}{10}\left[\frac{1}{E({}^4T_1(y))} - \frac{1}{E({}^4T_1(x))}\right] \quad (8D)$$

the spin Hamiltonian, E is the rhombic ZFS parameter, $\zeta_{Fe^{3+}}$ is

the effective spin–orbit coupling parameter for ferric iron ($\zeta_{Fe^{3+}} \approx 300$–$400$ cm^{-1}), and $E(^4T_1(i))$ are the energies of the low-symmetry split, orbital components of the first ligand-field excited $^4T_1$ state. In this model the zero-field splitting arises solely from the low-symmetry energy splitting of the $^4T_1$ state. The energies[36] of the components of the $^4T_1$ state are given by eq 9. The "+"

$$E(^4T_1(z)) = {}^4T_1(\text{cubic}) + \frac{2}{3}\left(\pm\delta \pm \frac{3}{4}\mu\right)$$
$$E(^4T_1(x)) = {}^4T_1(\text{cubic}) - \frac{1}{3}\left(\pm\delta \pm \frac{3}{4}\mu \pm \frac{3}{2}\alpha\right) \quad (9A)$$
$$E(^4T_1(y)) = {}^4T_1(\text{cubic}) - \frac{1}{3}\left(\pm\delta \pm \frac{3}{4}\mu - \left(\pm\frac{3}{2}\alpha\right)\right)$$

applies for complexes with the $^4T_1$, $e^3t_2^2$ lowest (i.e. T_d), while the "–" is appropriate for complexes with the $^4T_1$, $e^1t_2^4$ lowest (O_h and square pyramidal). δ, μ, and α are defined in eq 9B, where for example $E(d_{xy})$ is the energy of the d_{xy} orbital.

$$\delta = \frac{E(d_{xz}) + E(d_{yz})}{2} - E(d_{xy})$$
$$\mu = E(d_{x^2-y^2}) - E(D_{z^2}) \qquad \alpha = E(d_{yz}) - E(d_{xz}) \quad (9B)$$

Recently this model was tested[8] for two high-spin axially distorted tetrahedral ferric complexes ($FeCl_4^-$ and $Fe(SR)_4^-$), where the $^4T_1(i)$ states and the ZFS were determined experimentally. It was found that when the experimentally observed energies were used in eq 8 the calculated D had the wrong sign and magnitude. It was shown that this disagreement results from a neglect of covalency effects, which can be large for these tetrahedral systems. In particular it was found[1] that anisotropic covalency can account for the observed D.

Covalency causes a reduction in the magnitude of the spin–orbit coupling between the ground and excited $^4T_1(i)$ states. If the covalency is anisotropic then the different $^4T_1(i)$ components will spin–orbit couple to the ground state with different magnitudes. This amounts to inclusion of reduction factors[40] in eq 8A and 8C, leading to eq 10. The reduction factors κ are related to the covalency parameters of the complex as given in eq 11. β^2, ξ^2,

$$D = \frac{(\zeta_{Fe^{3+}})^2}{10}\left[\frac{2\kappa_z^2}{E(^4T_1(z))} - \frac{\kappa_y^2}{E(^4T_1(y))} - \frac{\kappa_x^2}{E(^4T_1(x))}\right] \quad (10A)$$

$$E = \frac{(\zeta_{Fe^{3+}})^2}{10}\left[\frac{\kappa_y^2}{E(^4T_1(y))} - \frac{\kappa_x^2}{E(^4T_1(x))}\right] \quad (10B)$$

$$\kappa_z^2 = (1-\beta^2)(1-\epsilon^2)$$
$$\kappa_x^2 = \left[\frac{\sqrt{(1-\xi^2)(1-\epsilon^2)}}{4} + \frac{3\sqrt{(1-\xi^2)(1-\theta^2)}}{4}\right]^2 \quad (11)$$
$$\kappa_y^2 = \left[\frac{\sqrt{(1-\eta^2)(1-\epsilon^2)}}{4} + \frac{3\sqrt{(1-\eta^2)(1-\theta^2)}}{4}\right]^2$$

η^2, ϵ^2, and θ^2 represent the amount of ligand character in the Fe d_{xy}, d_{yz}, d_{xz}, $d_{x^2-y^2}$, and d_{z^2} orbitals, respectively. Equations 10 and 11 were derived assuming that the ligand makes a negligible contribution to spin–orbit coupling and the geometry represents a simple distortion away from cubic symmetry (octahedral or tetrahedral). Equation 11 is based on the assumption that there is no mixing between the Fe 3d orbitals. This will affect the ZFS parameters and will be addressed later.

As was pointed out previously, anisotropic covalency[8] in the Fe d σ antibonding orbitals directly opposes the energy-splitting contribution to the ZFS. This is because the energy splitting of the $^4T_1$ state is linked to the covalency parameters as both depend on the interaction of the Fe d orbitals with the ligand valence orbitals. Therefore, the inclusion of anisotropic covalency in eq 8 reduces the magnitude of the calculated ZFS and can even cause it to change sign. This can be seen from a consideration of an axial distorted T_d complex. When δ is positive, then $E(^4T_1(z)) > E(^4T_1(x,y))$ (eq 9). If δ is positive the $d_{xz,yz}$ orbitals must have a stronger antibonding interaction with the ligands causing $\beta^2 < \eta^2, \xi^2$, and therefore $\kappa_z^2 > \kappa_{x,y}^2$ (eq 11). In the axial (i.e. $\kappa_z \neq \kappa_x = \kappa_y$) T_d ferric complexes studied it was found that the σ anisotropy in covalency dominated the ZFS and was responsible for determining the experimental sign of D. This occurs because the ZFS is more sensitive to small changes in the covalency parameters than to changes in the energy denominators in eq 10.

The covalency parameters and the Fe d orbital energies are related through perturbation theory, where the amount that an Fe d orbital is destabilized, ΔE, and the amount of ligand character, α^2_L, in the Fe 3d orbital is given by eq 12. H_{ML} is

$$\Delta E = \frac{E}{2}[\sqrt{V^2+1} - 1] \quad (12A)$$

$$\alpha_L^2 = \sin^2\left(\frac{\arctan(V)}{2}\right) \quad (12B)$$

$$V = \frac{2H_{ML}}{E} \quad (12C)$$

the interaction matrix element between the metal 3d orbital and the ligand orbital (i.e. symmetry adapted linear combination (SALC)), and E is the energy separation between the ligand valence SALC and the Fe 3d orbitals before interaction. The change in α_L^2 for the same change in ΔE is given by eq 13.

$$\frac{\partial\alpha_L^2}{\partial\Delta E} = \frac{E}{E^2 + 4H_{ML}^2} \quad (13)$$

Clearly the sensitivity of the ZFS to the anisotropic covalency will be greatest when the covalency parameters change rapidly for the same change in ΔE (i.e. $\partial\alpha^2_L/\partial\Delta E$ is large). From eq 13 this occurs when both E and H_{ML} are small.

V for the D_{2d} $FeCl_4^-$ complex can be estimated from SCF–Xα–SW calculations[41] from which α_L^2 is found to be 0.28 ($V = 2.04$). If E is set equal to $2E'$ then $H_{ML}(T_d) = 2.04E'$. In the Wolfberg–Helmholz approximation[42] H_{ML} is proportional to the group overlap of the ligand SALC with the Fe 3d orbitals; thus for the same ligand set $H_{ML}(T_d) = {}^4/_9 H_{ML}(O_h)$, therefore $H_{ML}(O_h) = 4.59E'$. In addition, E will be larger for an octahedral complex due to the greater electrostatic destabilization of the Fe 3d orbitals for 6 versus 4 ligands. At most, $E(O_h) = 1.5E(T_d)$. By using $E(T_d) = 2E'$, $E(O_h) = 3E'$, $H_{ML}(O_h) = 4.59E'$, and $H_{ML}(T_d) = 2.04E'$ in eq 13, it is found that α_L^2 changes 3 times faster for T_d complexes relative to O_h for the same change in ΔE. Therefore the ZFS in O_h complexes will be much less sensitive to anisotropic covalency. In addition, the κ's for O_h complexes are less sensitive to changes in covalency of the σ antibonding orbitals (eq 11, $\theta(d_{z^2})$ and $\epsilon(d_{x^2-y^2})$). Also the energy of the lowest $^4T_1$ state is smaller for O_h complexes than for T_d complexes because of the larger value for 10Dq. Thus for O_h complexes the ZFS will be more sensitive to changes in the energy denominators than will the corresponding T_d complexes.

With use of eqs 10, 11, and 12, D for both an octahedral and a tetrahedral complex is calculated assuming no anisotropy or energy splitting of the π antibonding Fe 3d orbitals (e for T_d and t_{2g} for O_h). From Xα–SW calculations[41] on the tetrahedral $FeCl_4^-$ the Fe 3d π (d_{z^2}, $d_{x^2-y^2}$) covalency is estimated to be 10% ligand character ($V_\pi = 0.75$, from eq 12B), while the Fe 3d σ (d_{xy}, d_{xz}, d_{yz}) covalency is estimated to be 28% ligand character ($V_\sigma = 2.04$). The value of 10Dq has been experimentally determined[8a] to be 6500 cm^{-1} for this complex, with the $^4T_1$ occurring at 14000 cm^{-1}. Using eqs 12A and 12B to calculate the difference in energy

(40) Stevens, K. W. H. *Proc. R. Soc. London* **1953**, *A219*, 542.

(41) Butcher, K. D.; Gebhard, M. S.; Solomon, E. I. *Inorg. Chem.* **1990**, *29*, 2067.

(42) Wolfberg, M.; Helmholz, L. *J. Chem. Phys.* **1952**, *20*, 837.

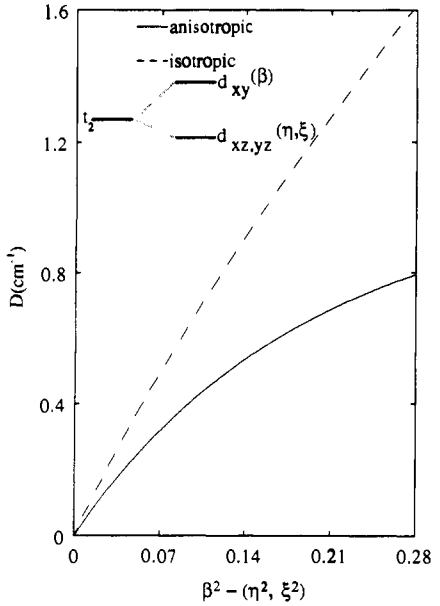

Figure 15. Effect of σ bonding anisotropy on D_{calc} for $FeCl_4^-$ (inset gives the t_2 d-orbital splitting).

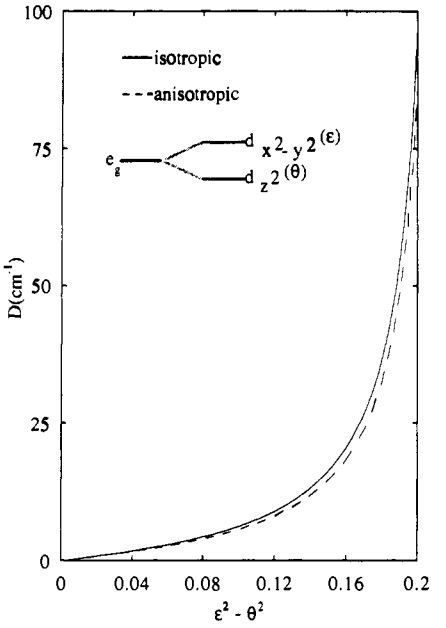

Figure 16. Effect of σ bonding anisotropy on D_{calc} for $FeCl_6^{3-}$ (inset shows the e d-orbital splitting).

destabilization of the Fe σ and π orbitals, i.e. 10Dq, gives eq 14 which allows E to be estimated as 12745 cm^{-1}. Figure 15 presents

$$10Dq = \frac{E}{2}[\sqrt{V_\sigma^2 + 1} - \sqrt{V_\pi^2 + 1}] \qquad (14)$$

D_{calc} as a function of $\beta^2 - \eta^2$, ξ^2, where the covalency and energy of the d_{xy} orbital are fixed, while reducing the energy and covalency of the $d_{xz,yz}$ set. D_{calc} with an isotropic κ (i.e. $\kappa_{av} = (\kappa_z + \kappa_{x,y})/2$) is also shown. As can be seen from Figure 15, inclusion of anisotropic covalency dramatically affects D_{calc} for the T_d complex.

Figure 16 presents D_{calc} as a function of $\epsilon^2 - \theta^2$ for a similar calculation on an O_h $FeCl_6^{3-}$ complex, with the only difference being a 9/4 increase in H_{ML} for the most antibonding Fe 3d orbital (i.e. $d_{x^2-y^2}$). As with the T_d calculation the Fe π covalency was held at 10% ligand character, while the covalency of the $d_{x^2-y^2}$ was held at 40%. As can be seen from Figure 16, D_{calc} is much less sensitive to anisotropic covalency than the corresponding tetrahedral calculation. Thus, the ZFS in O_h complexes mostly reflects the energy splitting of the Fe d σ orbitals ($d_{x^2-y^2}$ and d_{z^2}) due to the ligand field. $D > 0$ indicates that $E(d_{x^2-y^2}) - E(d_{z^2}) > 0$, while

Table III

Fe 3d orbital mixings	rotation of ZFS tensor[46]
d_{z^2}–d_{yz}	rotates D_{zz} toward D_{yy}
d_{z^2}–d_{xz}	rotates D_{zz} toward D_{xx}
$d_{x^2-y^2}$–d_{yz}	rotates D_{zz} toward D_{yy}
$d_{x^2-y^2}$–d_{xz}	rotates D_{zz} toward D_{xx}
d_{xy}–d_{xz}	rotates D_{zz} toward D_{yy}
d_{xy}–d_{yz}	rotates D_{zz} toward D_{xx}

$D < 0$ indicates that $E(d_{x^2-y^2}) - E(d_{z^2}) < 0$.

In the above treatment only axial contributions to the ZFS were considered. However, the ligand bound forms of Fe(+3)SBL exhibit a rhombic ZFS. This indicates that the site symmetry is lowered. If the Fe site symmetry is still orthorhombic (i.e. D_2) as in the case for the anion bound forms of Fe(+3)SBL, then a rhombic ZFS tensor can only arise[43] if there is an energy splitting between the d_{xz} and d_{yz} orbitals, which causes the $^4T_1(x)$ and $^4T_1(y)$ energy denominators to be different (eqs 9 and 10).

If the site symmetry is lower than D_2 (i.e. C_{2v}), then significant mixing of the orthorhombic states can also take place. Expressions for the spin–orbit matrix elements of eqs 8A and 8C in terms of the one electron Fe d orbitals have been derived by using the irreducible tensor method[44] and are given in eq 15

$$\langle {}^6A_1||H_{so}||{}^4T_1(x)\rangle = 3[1/2\langle d_{yz}|l_x|d_{x^2-y^2}\rangle - (3)^{1/2}/2\langle d_{yz}|l_x|d_{z^2}\rangle] \qquad (15A)$$

$$\langle {}^6A_1||H_{so}||{}^4T_1(y)\rangle = 3[1/2\langle d_{xz}|l_y|d_{x^2-y^2}\rangle + (3)^{1/2}/2\langle d_{xz}|l_y|d_{z^2}\rangle] \qquad (15B)$$

where l_x and l_y are the x and y orbital angular momentum operators, respectively. If the d_{yz} orbital mixes with the d_{z^2} orbital due to some lower than orthorhombic perturbation then the last term on the right of eq 15A will be reduced. That is if $\phi_1 = ad_{yz} + bd_{z^2}$ and $\phi_2 = ad_{z^2} - bd_{yz}$ then $\langle\phi_1|l_x|\phi_2\rangle = (a^2 - b^2)\langle d_{yz}|l_x|d_{z^2}\rangle$. Therefore this mixing will significantly reduce the $\langle {}^6A_1||H_{so}||{}^4T_1(x)\rangle$ matrix element as the last term on the right of eq 15A makes the dominant contribution. Analogously, this mechanism would reduce the $\langle {}^6A_1||H_{so}||{}^4T_1(y)\rangle$ matrix element (eq 15B) if d_{z^2} and d_{xz} mixing were to occur. Thus, selective mixing of the d_{z^2} orbital into the d_{xz} or d_{yz} orbital will reduce the associated spin–orbit matrix elements between the ground state and either the $^4T_1(y)$ or $^4T_1(x)$ excited states, causing $\langle {}^6A_1||H_{so}||{}^4T_1(x)\rangle \neq \langle {}^6A_1||H_{so}||{}^4T_1(y)\rangle$ in the numerators in eq 8C and producing a rhombic contribution to the ZFS tensor. This mechanism for a rhombic ZFS tensor can be distinguished from the alternative d_{xz},d_{yz} splitting mechanism as the latter will not rotate the ZFS tensor.

Mixing of the d orbitals also causes the ZFS tensor to be rotated off the orthorhombic coordinate system. In the orthorhombic system the ZFS tensor is required to have three perpendicular C_2 axes (i.e. x, y, and z lie along the bonds). The mixing of the d orbitals rotates the ZFS tensor as it results in non-zero off-diagonal elements[45] (D_{ij}, $i \neq j$) in the ZFS tensor as defined in the orthorhombic coordinate system. The off-diagonal D_{ij} are given in eq 16, where $S_i L_i$ and $S_j L_j$ are the i and j components

$$D_{ij} \propto \langle {}^6A_1|S_i L_i|{}^4T_1(h)\rangle\langle {}^6A_1|S_j L_j|{}^4T_1(h)\rangle \qquad (16)$$

of the spin–orbit operator. On the basis of eq 16, off-diagonal

(43) In D_2 or C_{2v} symmetry the d_{z^2} and $d_{x^2-y^2}$ orbitals can mix. This will reduce the magnitude of the spin–orbit coupling matrix element between the $^6A_1$ ground state and the x and y orbital components of the $^4T_1$ ligand field excited state; however, this will affect both $\langle {}^6A_1||H_{so}||{}^4T_1x\rangle$ and $\langle {}^6A_1||H_{so}||{}^4T_1y\rangle$ equally (i.e. $\kappa_x = \kappa_y$), and thus cannot produce a rhombic ZFS.

(44) Piepho, S. B.; Schatz, P. N. *Group Theory in Spectroscopy with Applications to Magnetic Circular Dichroism*; Wiley: New York, 1983.

(45) Note the D_{ij} are elements of the ZFS tensor and should not be confused with the D from the spin Hamiltonian in eq 1.

(46) The rotations are referenced to the orthorhombic coordinate system for the ZFS tensor, D_{ii}. The other possible d orbital mixings cannot cause the principal axis of the ZFS tensor to be rotated away from the z axis, but they will cause the tensor to be rotated about the z axis (i.e. mixing x and y). The mixing of the d_{z^2} and $d_{x^2-y^2}$ orbitals can rotate the ZFS tensor, but only 90° (i.e. exchanging the x or y axis with the z axis).

elements will be present in the ZFS tensor only if a given $^4T_1(h)$ ($h = x, y$, or z) component can spin–orbit couple to the ground state through both S_iL_i and S_jL_j ($i, j = x, y$, or z; $i \neq j$). Table III gives the d orbital mixings, which rotate the ZFS tensor, and the rotation direction relative to the orthorhombic coordinate system. These were determined with use of the irreducible tensor method[43] to evaluate the above D_{ij} matrix elements in terms of the one-electron d orbitals. As can be seen from Table III the mixing of the d_{z^2} orbital into either the d_{xz} or d_{yz} orbital not only produces a rhombic ZFS but also rotates the ZFS tensor.

The mixing of the d orbitals can also be used to provide structural information on the ligand environment about the Fe(+3). In particular, the origin of the d_{z^2} mixing into the d_{xz} or d_{yz} orbital can be evaluated by using the ligand-field expressions of Companion et al.[47] which relate the energy splittings and mixing of the d orbitals to geometric parameters of the complex. The mixing of the d_{z^2} into the d_{xz} or d_{yz} orbitals is determined by the magnitude of the off-diagonal matrix elements given below:

$$H_{z^2,yz} = \sum_i C_1(\sin\theta_i \cos\theta_i \sin\phi_i) + C_2(\sin\theta_i \cos\theta_i \sin\phi_i((7\cos^2\theta_i/3) - 1))$$

$$H_{z^2,xz} = \sum_i C_3(\sin^2\theta_i \sin 2\phi_i) + C_4(\sin^2\theta_i \sin 2\phi_i(7\cos^2\theta_i - 1)) \quad (17)$$

where the sum is over all ligands (i), θ is the angle between the ligand and the z molecular axis, and ϕ involves a rotation about the molecular z axis. Both matrix elements in eq 17 are required to be zero for six ligands at the vertices of an octahedron. In fact, a significant off-diagonal element will only occur if a ligand is placed along a direction off the octahedral bond directions (i.e. $\theta = 45°$, $\phi = 90°$). Therefore, if addition of a ligand to an axial six-coordinate Fe(+3) site causes the ZFS tensor to become rhombic and rotate, then this ligand must induce significant geometric distortions, likely binding as a seventh ligand.

On the basis of the above analysis, the observed positive and axial ZFS of the native Fe(+3)SBL indicates that the $d_{x^2-y^2}$ is more destabilized than the d_{z^2} orbital. This means that the strong field ligands (i.e. histidine) must lie in the x,y plane as defined by the ZFS coordinate system. This is consistent with the determination that the His → Fe(+3) CT transitions are x,y polarized relative to the **g** tensor as defined by the ZFS coordinate system. The lack of a rhombic contribution indicates that the splitting of the d_{xz} and d_{yz} orbitals must be very small, and that the mixing of the Fe 3d orbitals is negligible. Upon binding OCN^-, the observed ZFS becomes rhombic but the ZFS does not rotate (from the analysis of the MCD saturation data) and thus the Fe(+3) site remains six coordinate. This indicates that binding OCN^- to the native site does not induce mixing of the d orbitals, and therefore the rhombic ZFS arises from a significant splitting of the d_{xz}, d_{yz} orbitals consistent with the MCD analysis indicating that N_3^- (and therefore OCN^-) binds approximately in the equatorial plane.

Discussion

MCD and EPR spectroscopies have been used to elucidate geometric and electronic structural features of a high-spin ferric site which does not have the advantage of the high symmetry associated with heme or iron sulfur proteins. Low-temperature MCD probes the selection rules associated with ligand-field and CT excited states while its temperature dependence complements EPR studies in determining the ZFS of the ground state. Together these techniques allow one to obtain the effective geometry at the ferric site, to determine the orientation of chromophoric ligands relative to the ZFS tensor, and to define the specific structural features associated with the ligand-field origin of the ZFS.

Low-temperature MCD spectroscopy has enabled the observation of the spin-forbidden LF transitions at energies below the onset of intense CT features at ~500 nm. These d → d transitions are too weak to be observed in absorption spectroscopy but provide important insight into the ligand field as determined by the geometric structure of the ferric site. The region between 500 and 1100 nm contains two ligand-field transitions, $^6A_1 \rightarrow {}^4T_1$ and $^6A_1 \rightarrow {}^4T_2$, with the latter at higher energy. The C-term signs and energies are determined by the geometry of the ferric site and are summarized for a series of structural types in Table II. Tetrahedral ferric complexes exhibit a low energy negative and higher energy positive C term while octahedral and square-pyramidal complexes exhibit a low energy positive and higher energy negative C term. The latter two complexes can be distinguished on the basis that in a square-pyramidal complex the MCD active components of the $^6A_1 \rightarrow {}^4T_1$ and $^6A_1 \rightarrow {}^4T_2$ transitions should be at lower and higher energy, respectively, as compared to the equivalent transitions in octahedral complexes. Trigonal-bipyramidal and seven-coordinate complexes both exhibit two positive C terms in this region. These can, however, be distinguished on the basis of their energies as the seven-coordinate complex will have its lowest energy positive feature at ~12 000 cm^{-1} as compared with 14 000 cm^{-1} in the trigonal-bipyramidal complex. Finally, it should be noted that the spin-forbidden transitions in high-spin ferric complexes are still weak in the low-temperature MCD spectrum and one must be careful to distinguish these from contributions due to heme and ferrous impurities.

MCD studies in the CT region have particularly emphasized the saturation behavior of the C terms to obtain the polarization of the transitions. Since in low-symmetry non-heme iron active sites the L → Fe(+3) CT transitions will be polarized approximately along the ligand–metal bond, this can provide information on the orientation of this bond relative to the **g** tensor of the ground doublet which in turn is defined by the ZFS. C-term MCD intensity requires two perpendicular transition moments, and in these low-symmetry complexes two possible mechanisms have been considered for the C-term intensity associated with the L → Fe(+3) CT transitions. First, there can be more than one ligand of the same type providing transition moments which are at very similar energies. If two ligand–Fe(+3) bonds are perpendicular they will produce an x,y polarized transition in the coordinate system defined by these ligand–iron bonds. If the ZFS tensor is oriented collinear with this transition moment tensor, then the MCD saturation data are accurately described by the first term in eq 6, where the experimental g values of the ground doublet are used. This appears to be the case for the 350-nm His → Fe(+3) CT transition in native Fe(+3)SBL in Figure 10. If the saturation magnetization data cannot be fit by the experimental g values, this indicates that either the ZFS tensor is rotated relative to the transition moment tensor or the g_{unique} direction used as g_z is not along the z axis. The latter occurs for a rhombic (i.e. orthorhombic) positive ZFS tensor because g_{unique} is perpendicular to the z direction. A method has been employed to treat this problem in the coordinate system defined by the transition moment tensor. Still using the first term in eq 6 for an x,y-polarized transition, the experimental **g** tensor is rotated and projected onto the transition moment tensor until a reasonable fit is obtained to the data. This approach has been used to fit the data for the Fe(+3)SBL–OCN^- complex. Here the 350-nm endogenous His → Fe(+3) CT transitions, which were determined to be x,y polarized in the native enzyme, saturate with an effective g value which indicates that the $g = 9.44$ direction now lies in the x,y plane defined by the histidines. A second mechanism is required for the C-term MCD intensity for a CT transition associated with a single ligand–metal bond. This is a unidirectional transition (along the ligand–metal bond) and one must invoke spin–orbit mixing of intensity from other CT states into this transition to induce a perpendicular transition moment. If one reasonably assumes this mixing is small and approximately isotropic, then this problem can be described by using the second term in eq 6, where now the z axis is defined along the dominant transition moment which is along the chromophoric ligand–Fe(+3) bond. This procedure works even for the rhombic case because both the transition moment tensor and the spectral g values are effectively axial (but potentially with different orientations of their unique direction). Again if this expression does not fit the data for a unidirectional transition with the experimental g values of the

(47) Companion, A. L.; Komarynsky, M. A. *J. Chem. Educ.* **1964**, *41*, 257.

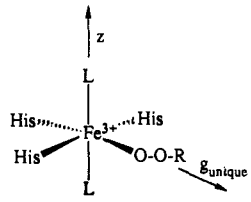

Figure 17. Spectroscopic effective model for hydroperoxide product binding to the Fe(+3)SBL active site. Z and g_{unique} = 9.44 define the axes of the ZFS tensor.

ground doublet, it is an indication that the transition moment and ZFS tensors are not collinear, with their relative angle estimated by the projection of the experimental **g** tensor on the transition moment tensor. This treatment was required for the data on the Fe(+3)SBL–N_3^- complex presented in Figure 14. As a general approach one employs eq 6 to fit the MCD associated with a given CT transition using the experimental g values. A poor fit indicates a rotation of the ZFS tensor relative to the transition moment tensor. If the polarization of the transition is known, as is the case for the complexes studied above, then one can determine the relative rotation of the tensors.

As one of the most generally measured spectral properties of high-spin ferric complexes is the ZFS of the ground state, we have been particularly interested in understanding the ligand-field and structural origins of the ZFS. While in distorted tetrahedral complexes we have found this to be dominated by anisotropic covalency effects, for octahedral and 5-coordinate complexes we find that the anisotropic covalency effect on the ZFS is quite small and that the ZFS is dominated by the splittings and mixings of d orbitals. The sign and magnitude of the axial ZFS, D, is determined by the relative order and extent of splitting of the $d_{x^2-y^2}$ and d_{z^2} orbitals. A positive D corresponds to the d_{z^2} being lowest in energy which would result from a distortion of an octahedron such that the axial z direction has a weak ligand field. A rhombic ZFS of the ground state can derive from two possible orbital effects. First, a splitting of the degeneracy of the d_{xz} and d_{yz} orbitals will change the energy denominators in eq 8 and produce an orthorhombic ZFS (i.e. one which does not rotate the z axis). The second orbital origin of rhombic splitting involves a mixing of the d_{z^2} into the d_{xz} (or d_{yz}) orbital which reduces the spin–orbit matrix elements in eq 8 and additionally has the effect of rotating the z axis of the ZFS tensor. Ligand-field theory indicates that this off-diagonal mixing in octahedral complexes requires a contribution to the ligand field (eq 17) from a ligand not oriented along the octahedral L–M bonds.

Thus our studies of Fe(+3)SBL has shown that oxidation of the octahedral Fe(+2) site produces little change in the coordination sphere of the iron center. From the x,y polarization of the His → Fe(+3) CT transition combined with EXAFS studies[18,20] there appear to be at least three His ligands all coordinated in an equitorial plane. These His ligands define the x,y plane, and the origin of the positive ZFS of native Fe(+3)SBL derives from these strong field ligands destabilizing the $d_{x^2-y^2}$ relative to d_{z^2} orbital. EPR studies show that anion binding results in a rhombic EPR signal, and the saturation behavior of the MCD signal of the OCN^- complex demonstrates that the actual ZFS tensor remains oriented as in the native enzyme. As summarized above, this requires that the exogenous ligand splits the d_{xz} d_{yz} orbital set, indicating that it replaces one of the ligands in the x,y plane consistent with the N_3^- binding orientation determined from the saturation magnetization data. These exogenous ligands perturb the EPR spectrum of the active site in a manner that parallels the organic hydroperoxide product interaction with the ferric protein site. The presence of an N_3^- → Fe(+3) CT transition requires that the exogenous ligand binds directly to the Fe(+3) causing the rhombic perturbation. Addition of the hydroperoxide product to Fe(+3)SBL results in an absorption band at 570 nm which, based on spectral correlations to the exogenous L → Fe(+3) CT transitions for N_3^-, OCN^-, and HOO^- bound forms of met hemerythrin, should be a peroxide → Fe(+3) CT transition. This suggests that the organic hydroperoxide binds to the Fe(+3) center in a manner analogous to that of N_3^- as shown in Figure 17. This model of the product peroxide binding directly to the Fe(+3) relates to the two mechanistic proposals in the literature. Corey et al.[17b] have suggested that an organometallic Fe(+3)–substrate bond is involved, which would simply require insertion of O_2 to form the product in Figure 17. The alternative mechanism involves the substrate reducing the iron site to form an Fe(+2) and an adjacent substrate radical.[17a] As we have found that the ferrous site in SBL does not bind anions,[4,48] this mechanism would appear to involve the presence of bound substrate radical activating the ferrous center for intersphere reactivity with O_2. Having defined an MCD approach to the study of Fe(+2) and Fe(+3) sites, these two mechanisms could be tested experimentally. In addition, the application of the above approach to the study of non-heme ferric enzyme active sites and their interactions with exogenous ligands should be useful in obtaining structural information on the molecular mechanism of other enzymes for which the ferric site has been implicated in catalysis.

Acknowledgment. This work was supported by the National Institutes of Health (Grant No. GM40392). Y. Zhang also gratefully acknowledges the assistance of Dr. James Whittaker in the initial stages of this research.

(48) It should be noted that Fe(+2)SBL reversibly reacts with NO, but not O_2, F^-, or N_3^-. (Galpin, J. R.; Veldink, G. A.; Vliegenthart, J. F. G.; Boldingh, J. *Biochim. Biophys. Acta* **1978**, *536*, 362, ref 4.)